## RESEARCH OUTPUTS / RÉSULTATS DE RECHERCHE

**Geological and geochemical constrains on the genesis of the sedimentary-hosted Bou Arfa Mn(-Fe) deposit (Eastern High Atlas, Morocco)**

Lafforgue, Ludovic; Dekoninck, Augustin; Barbarand, Jocelyn; Brigaux, Benjamin; Bouabdellah, Mohammed; Verhaert, Michele; Mouttaqi, Abdellah; Yans, Johan

# Journal Pre-proofs

Geological and geochemical constrains on the genesis of the sedimentary-hosted Bou Arfa Mn(-Fe) deposit (Eastern High Atlas, Morocco)

Ludovic Lafforgue, Augustin Dekoninck, Jocelyn Barbarand, Benjamin Brigaud, Mohammed Bouabdellah, Michèle Verhaert, Abdellah Mouttaqi, Johan Yans

Please cite this article as: L. Lafforgue, A. Dekoninck, J. Barbarand, B. Brigaud, M. Bouabdellah, M. Verhaert, A. Mouttaqi, J. Yans, Geological and geochemical constrains on the genesis of the sedimentary-hosted Bou Arfa Mn(-Fe) deposit (Eastern High Atlas, Morocco), *Ore Geology Reviews* (2021), doi: https://doi.org/10.1016/j.oregorev.2021.104094

This is a PDF file of an article that has undergone enhancements after acceptance, such as the addition of a cover page and metadata, and formatting for readability, but it is not yet the definitive version of record. This version will undergo additional copyediting, typesetting and review before it is published in its final form, but we are providing this version to give early visibility of the article. Please note that, during the production process, errors may be discovered which could affect the content, and all legal disclaimers that apply to the journal pertain.

1 **Geological and geochemical constrains on the genesis of the sedimentary-hosted Bou**

2 **Arfa Mn(-Fe) deposit (Eastern High Atlas, Morocco)**

3 Ludovic Lafforgue[1], Augustin Dekoninck[2,@], Jocelyn Barbarand[1], Benjamin Brigaud[1],

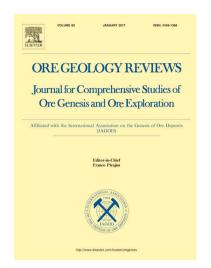4 Mohammed Bouabdellah[3], Michèle Verhaert[2], Abdellah Mouttaqi[4], Johan Yans[2]

5 [1]Université Paris-Saclay, CNRS, GEOPS, 91405, Orsay, France.

6 [2]Institute of Life-Earth-Environment (ILEE), University of Namur, 61 rue de Bruxelles B-5000,

7 Namur, Belgium.

8 [3]Département de Géologie, Faculté des Sciences, Université Mohammed Premier, Avenue

9 Mohammed VI, BP 717, 60000 Oujda, Morocco.

10 [4]Office national des Mines et des Hydrocarbures, BP 99 Rabat, Morocco.

11 Ludovic Lafforgue: ludovic.lafforgue.c@gmail.com

12 Augustin Dekoninck (corresponding author): augustin.dekoninck@unamur.be

13 Jocelyn Barbarand: jocelyn.barbarand@u-psud.fr

14 Benjamin Brigaud: benjamin.brigaud@u-psud.fr

15 Mohammed Bouabdellah: mbouabdellah2002@yahoo.fr

16 Michèle Verhaert: michele.verhaert@hotmail.com

17 Abdellah Mouttaqi: MOUTTAQI@onhym.com

18 Johan Yans: johan.yans@unamur.be

19

21 <u>Abstract</u>

22 Carbonate-hosted Mn deposits are widespread in North Africa with most of the Mn ores
23 being hosted by Mesozoic dolomitic formations of the Moroccan Atlasic system. The Bou
24 Arfa Mn(-Fe) deposit described herein is located in the eastern High Atlas, close to the North
25 Atlasic Front, and has accounted for the production of ~2 Mt of ore grading from 33 to 82%
26 Mn. The mineralization occurs within Sinemurian flat-lying dolostones as stratabound and
27 karst-filling (veins, lenses, pockets). This mineralization is characterized by the extensive
28 presence of pyrolusite, and minor concentrations of manganite, hausmannite, goethite and
29 hematite. Previous studies suggested that the Bou Arfa Mn-bearing mineralization has a
30 strictly synsedimentary origin, but the intense dolomitization and the occurrence of Mn oxides
31 instead of Mn carbonates question this model. New petrographical, mineralogical and
32 geochemical data show that three dolomitization phases accompanied the ore formation. The
33 early synsedimentary dolomitization was not responsible for strong Mn enrichments, whereas
34 a second dolomitization took place with the formation of hausmannite and manganite during
35 early diagenesis. The precipitation mechanism involves circulation of dissolved $Mn^{2+}$ in pore
36 waters, and then precipitation under diagenetic suboxic and alkaline conditions. The scarcity
37 of Mn carbonates is likely due to competitiveness of dissolved carbonates species that have
38 favored dolomite precipitation in the early stage. Presence of saddle dolomite in a
39 subsequent alteration stage, crystallography of the Fe oxides, and evolution of $\delta^{13}C$ and $\delta^{18}O$
40 reflect burial diagenesis and fluid mixing in the carbonate host rock. These conditions have
41 enabled the transformation of the primary ore into pyrolusite, when diagenetically-derived
42 hydrothermal fluids have generated vein-filling ore. The position of the Bou Arfa site above a
43 paleohigh formed during Atlas rifting, the presence of a faulted zone and the dolomitization of
44 the Sinemurian series have delimited the extension of this diagenetic Mn deposit, which is in
45 some points similar to MVT deposits of North Africa. Weathering is poorly recorded in the
46 Bou Arfa Mn ores due to the stability of the ore-forming minerals under subaerial conditions
47 in relation to the most recent periods of exposure of the High Atlas building.

2

## 1. INTRODUCTION

Sedimentary-hosted Mn deposits are considered as the most significant amongst different ore deposit types, because they ensure high longevity, large tonnage, and relatively high average grades (Kuleshov, 2016; Laznicka, 1992; Maynard, 2014; Roy, 2006). The accumulation of Mn in sediments is generally triggered by the formation of (i) ferromanganese nodules above the ocean floor (Glasby, 2006; Maynard, 2014; Wang and Müller, 2009), or (ii) Mn-bearing carbonates under diagenetic conditions, either from precipitation in pore waters, or by replacement of Mn-rich oxides, oxyhydroxides and hydroxides (hereafter referred to as Mn oxides; Johnson et al. 2016). Mn sources in sediments can be either distant hydrothermal vents or hydrogenous (terrigeneous) influxes (Fleet, 1983; Glasby, 2006). Formation models (Calvert and Pedersen, 1996; Cannon and Force, 1983; Force and Cannon, 1988; Force and Maynard, 1991; Maynard, 2014, 2010) involve the precipitation of primary Mn oxides at the interface between reducing and oxidizing environments. Most of these oxides are not deposited in deep sediments because they are dissolved again once they deepen in the water column, unless the seafloor is shallow enough to intercept the redox boundary. Iron is not involved in this process as Fe remains fixed in sulfide minerals at the deeper water-sediments interface (Maynard, 2014, 2010). Sea level changes may have a strong influence on the concentration and the geometry of Mn orebodies (Roy, 2006). Most of the sedimentary-diagenetic Mn deposits are hosted in C-rich shales and pelites (Kuleshov, 2016, 2011; Roy, 2006).

The Bou Arfa Mn deposit of the eastern High Atlas of Morocco (Fig. 1A) is located at the junction between the High Atlas and the High Plateau domain close to the North Atlasic Front (Fig. 1B). The Bou Arfa mineralization was discovered in 1912 and is the third Mn district of Morocco alongside the Imini-Tasdremt (Dekoninck et al., 2016a, 2020; Gutzmer et al., 2006) and the Ouarzazate mining districts (Choubert and Faure-Muret 1973; Pouit 1980; Fig. 1A). Previous works have shown that mineralization mainly occurs as stratabound and karst-fill within Sinemurian dolostones (Fig. 2). Their mineralogy consists exclusively of Mn oxides such as pyrolusite ($\beta$-$MnO_2$; Pouit and Jouravsky 1965). Vein-related Mn mineralization is also described and displays massive Fe oxides (goethite) alongside the Mn oxides. The dolomitized host rocks are enriched up to 1–3% Mn and Pouit and Jouravsky (1965) suggested that the carbonate host rocks constitute the source of manganese.

These features interestingly suggest the intervention of processes different from those involved in giant sedimentary-diagenetic deposits (Johnson et al., 2016; Kuleshov, 2016; Maynard, 2014, 2010; Roy, 2006). These high-grade Mn ores occurring in a restricted area would imply epigenetic processes related to dolomitization. Pouit and Jouravsky (1965)

85   suggested a two-step model to explain the evolution of the Mn mineralization after
86   replacement of a synsedimentary carbonate precursor and their oxidation. However, this
87   model remains questionable (du Dresnay, 1965; Michard and Raddi, 2011; Pouit and
88   Jouravsky, 1965). Accordingly, the genesis of Bou Arfa Mn mineralization needs an in-depth
89   revision in order to address issues related to the syn-sedimentary, diagenetic and/or
90   hydrothermal origin of the orebodies; the link with dolomitization of the host Sinemurian
91   marine carbonates; the massive presence of Mn oxides instead of Mn-rich carbonates
92   (kutnohorite, rhodochrosite or Mn-rich calcite) and the role played by supergene processes.
93   The main objectives of this paper consist of (1) refining the mineralogy and petrography of
94   the Mn mineralization and host carbonates, and (2) defining the relation between the ore
95   formation and host carbonates. The final aim is to propose a robust metallogenic model for
96   the Bou Arfa deposit and special care is devoted to the link between mineralization and
97   dolomitization.

## 2. REGIONAL AND LOCAL GEOLOGICAL SETTING

99   The Atlasic fold and thrust belt is a complex structure resulting from the inversion of Triassic
100  and Jurassic basins in the frame of the Africa-Europe convergence (Choubert and Faure-
101  Muret 1962; Mattauer et al. 1977; Fig. 1A). Two main faults border the chain: the northern
102  main thrust named the "North Atlasic Front" (NAF) and the "South Atlasic Fault" (SAF). The
103  chronology of the Atlasic building follows two main phases: Eocene and Plio-Quaternary
104  (Frizon de Lamotte et al., 2009, 2000). A third Miocene phase is identified due to lithosphere
105  thinning that supports the current topography of the Anti-Atlas, the High and the Middle Atlas
106  (Gouiza et al., 2017, 2017; Leprêtre et al., 2015; Missenard et al., 2008, 2006; Seber et al.,
107  1996).

108         The Bou Arfa area is located in the eastern part of the High Atlas, close to the NAF.
109  The host rocks correspond to Paleozoic schists undetermined in age unconformably overlain
110  by a thick pre-rift Triassic succession, and Jurassic and Cretaceous syn-rift sediments. The
111  Jbel Bou Arfa (1830m; Fig 1B) forms an E-W anticline crossed by a major E-W fault (Aïn
112  Beida fault; du Dresnay 1965). This structure separates the Atlasic system in the south from
113  a non-deformed domain forming the so-called "High Plateaus" in the north (Fig. 1B). Triassic
114  to Jurassic Atlasic basins are rift basins controlled by normal faults and represent transfer
115  zone between two opening domains, namely the Central Atlantic and Tethyan oceans (Fig.
116  1A; Frizon de Lamotte et al. 2000). The E-W Aïn Beida fault is a main regional structure that
117  split the Bou Arfa area in two blocks: the northern block hosts the Ain-Beida and Hamaraouet
118  Mn mineralization, whereas the southern block hosts small Mn spots (Fig. 1B).

119   In the Bou Arfa Mn deposit, Sinemurian series are dolostones interbedded with clays
120   and thin gypsum-rich sandstones (Choubert and Faure-Muret 1962; du Dresnay 1965;
121   Salahane 1978; Fig. 2). Two main dolostone units are observed (Fig. 2). The bottom
122   dolostone called Lower "Chocolate" Unit (LCU) because of its dark brownish color is a few
123   meters thick and displays clayey levels in the upper part (du Dresnay 1965; Fig. 2). The
124   second unit, called the Upper "Chocolate" Unit (UCU), is a massive dolostone composed of
125   several strata hosting evaporitic levels, with a cumulated thickness increasing from west to
126   east (10 to 30 meters thick; du Dresnay 1965). Both are separated by an arkose level. In Bou
127   Arfa, the Pliensbachian unit unconformably overlays the Sinemurian rocks with 180 m to
128   200 m of arkoses, in which granitic boulders are observed (Fig. 2).

129   The Lower Cretaceous rocks are only observed north of the NAF and form a thin
130   reddish detrital layer. Cretaceous limestones few meters thick form the Kif El Hamar relief
131   and corresponds to an E-W syncline following the Aïn Beida Fault (Fig. 1B). No Mn deposit is
132   observed in these two reliefs but Pb-Zn-Cu-V mineralization have been described (Fig. 1B;
133   Verhaert et al. 2017, 2018). Cenozoic conglomeratic lenses outcrop close to the Aïn Beida
134   Fault (Fig. 1B). These lenses are witnesses of the late Cenozoic activity of the Aïn Beida
135   Fault (Lafforgue, 2016).

136   **3. MATERIAL AND ANALYTICAL METHODS**

137   *3.1. Sampling strategy and methodology*

138   The Hamaraouet cliff offers a large domain of outcrops, where most of the samples were
139   collected (Fig. 1B). Mineralized orebodies and host rocks were sampled in the Hamaraouet
140   area (H1 to H4, 26 samples), in the gallery 63 (HB1, 3 samples) and in the Aïn Beida site (6
141   samples; Fig. 1B; Table 1). Reference stratigraphic log and host rock samples are described
142   in barren carbonates at Hamaraouet, where neither Fe, nor Mn oxides were observed (Fig.
143   2).

144   *3.2. Analytical methods*

145   The petrography of the samples was carried out using optical microscopy,
146   cathodoluminescence (CL) microscopy (OPEA), scanning electron microscopy (SEM) and
147   Raman-microspectrometry on 70 thin sections prepared in the GEOPS laboratory (Orsay,
148   France). The description of hand specimens (Table 1) was used to select representative
149   samples for geochemical analyses and specific mineral phases from the different stages
150   defined in the paragenesis. ICP-AES and ICP-MS on bulk samples and EPMA on individual
151   minerals were used for the geochemistry. Carbon and oxygen isotope geochemistry

152 performed on carbonate phases (calcite and dolomite) was undertaken to characterize the

153 source and evolution of paleofluids.

154 3.2.1 Petrography

155 Thin sections were observed with an optical microscope Leica at a magnification between

156 x25 and x100 in plane polarized light (PPL) and in cross-polarized light (CPL).

157 Cathodoluminescence observations were made with a *Cathodyne* platine under an

158 acceleration voltage of 10 to 15 kV and a current intensity from 250 to 400 mA. Exposure

159 time was approximately 800 msec for dolomite and seconds for calcite. Texture and optical

160 characteristics have been used to define the different dolomite phases in the mineralized

161 zone. A SEM Phillips XL30 coupled with an Energy Dispersive Spectrometer (EDS) detector

162 Synergie4 PGT was used for petrographical observations and semi-quantitative analyses

163 under an acceleration potential from 15 to 25 kV and probe current of 1.5 nA.

164 3.2.2 X-ray diffraction (XRD)

165 XRD analyses were used to distinguish or correlate mineral phases, especially

166 pyrolusite and Fe oxyhydroxide mineral species. XRD data were acquired in the GEOPS

167 laboratory using a PANalytical X'Pert PRO diffractometer with X'Celerator detector and a

168 copper anticathode providing Cu $K\alpha_1$ emission ray. A Ni filter of 0.02 mm was used upon the

169 receptor. Analyses were realized on disoriented powder. All results were treated with X'pert

170 HighScore 3.0e in order to avoid induced $K\alpha_2$ rays.

171 3.2.3 Raman microspectrometry

172 Raman microspectrometry analysis was carried out at the University of Lille 1 (France)

173 in the CGCE laboratory. A Horiba Jobin-Yvon spectrometer equipped with an $Ar^+$ laser was

174 used with a wavelength of 532 nm. A long acquisition time was needed for Mn oxyhydroxides

175 (~30 sec; Julien et al. 2004; Gao et al. 2009). The Ar laser spot size was between 1–2 μm

176 with variable power (max 92 mW). A filter (D1) was used in order to limit the power at

177 9.2 mW and in order to avoid phase changes due to the laser power. Raman spectra were

178 further treated with the CrystalSleuth software using the Rruff database. Peak parameters

179 were obtained with pseudoVoigt modelisation with fityk 0.8.0 software.

180 3.2.4 Geochemistry

181 *3.2.4.1 Bulk-rock analysis*

182 Twenty-five samples were analyzed as powders after crushing with an agate mortar at the

183 SARM laboratory (Nantes, France). An ICP-AES Jobin-Yvon JY 70 Type II was used for

6

184    major elements (Si, Al, Fe total, Mn total, Mg, Ca, Na, K, P, Ti and LOI). Trace elements and

185    rare earth elements were analyzed with an ICP-MS Perkin Elmer ELAN 5000 (Tables 2 and

186    3). Samples were heated at 1000 °C (fire loss) and then treated by Li tetraborate fusion to

187    determine the Lost On Ignition (LOI). Samples were analyzed after an acid dissolution (ICP-

188    AES) or a dilution (ICP-MS). Standards were routinely analyzed under the same procedure.

189    The data were compared to the Upper Continental Crust composition (Mc Donough and Sun,

190    1995) to show up enrichment or depletion. This standard was chosen as it represents the

191    best approximation for the types of rock involved in the mineralizing process at Bou Arfa.

192    *3.2.4.2 Electron Probe Microanalysis*

193    An Electron Probe Microanalysis (EPMA) CAMECA SX-Five was used for quantitative

194    analyses at the University Pierre-et-Marie-Curie of Paris (UPMC) in the Camparis Service.

195    EPMA is equipped with a $LaB_6$ source and five Wavelengths Dispersive Spectrometers

196    (WDS) coupled with a Bruker EDS. Acceleration potential was 15 kV and variable probe

197    current were used for the identification of minor (low current) and major elements (high

198    current). Standards and probe current are indicated in the data repository (DR1). Analyses

199    were performed on the different dolomite generations (210 spots), on the Mn (217 spots;

200    pyrolusite, hausmannite, cryptomelane, hollandite and chalcophanite) and the Fe (105 spots;

201    hematite and goethite) oxides (Tables 4, 5 and 6).

202    3.2.5 Stable Isotope geochemistry

203    The $\delta^{13}C$ and $\delta^{18}O$ compositions of carbonates were obtained at the Radiometric Dating and

204    Stable Isotope Research laboratory at the University of Kiel (Germany). Samples were

205    formerly collected using a micro-drill tool after an in-depth cathodoluminescence

206    characterization. Carbon and oxygen isotopic compositions were determined using 100%

207    $H_3PO_4$ dissolution at 75 °C with a prototype Kiel 1 unit attached to a Thermo Finnigan MAT

208    251 mass spectrometer. The results are given in the standard δ-notation, which is expressed

209    relative to V-PDB (Vienna Pee Dee Belemnite) for carbon isotopes and V-SMOW (Vienna

210    Standard Mean Ocean Water) for oxygen isotopes in permil (‰; Table 7). The reproducibility

211    of the analyses of in-house standards gave an external precision (1SD) of ± 0.02‰ for $\delta^{18}O$

212    and 0.01‰ for $\delta^{13}C$.

213    **4. RESULTS**

214    *4.1 Dolomitization*

215    Dolomitization is the main form of wall-rock alteration and three stages are distinguished: (i)

216    extensive syn-sedimentary to early diagenetic replacement dolomite, (ii) epigenetic ore-stage

217 and (iii) hydrothermal dolomite superimposed on the diagenetic dolostone (Fig. 4). Regional

218 dolomitization predates mineralization and significantly enhances porosity and permeability

219 of the host rock. Ore-related dolomites occur as pore-filling or veins crosscutting the host

220 dolostone.

221   4.1.1 Barren Upper Chocolate Unit (UCU)

222     Three facies are recognized in the Upper Chocolate Unit (UCU; from bottom to top): (i)

223 sandy dolostone, (ii) massive fine-grained dolostone and (iii) bedded dolostone with bird

224 eyes (Fig. 2). (i) The UCU starts with a thin level (<50 cm thick) displaying a high proportion

225 of detrital elements including quartz, K-feldspar, and muscovite with subordinate apatite and

226 Ti oxides. These elements are cemented by an anhedral coarse-grained dolomite (Fig. 3A).

227 CL exhibits a red color in the dolomite crystals. (ii) The main facies of the UCU, where most

228 of the ore is located, is formed by a massive dolostone. The lower facies consists of a coarse

229 dolostone where sedimentary textures (pellets, ooliths and pisoliths) are partly preserved

230 (Fig. 3B), and partially replaced by well-developed cloudy microsaccharoïdal to millimetric

231 planar dolomite crystals (Fig. 3C). Pisoliths have a single to multiple-nuclei structure with

232 lightly colored columnar microbial laminations. No Mn- or Fe-rich ooliths (or nodules) nor

233 laminations are observed. (iii) In the upper facies of the UCU, bird eyes are the main feature

234 (Fig. 3D). This level is composed of a micritic brownish dolomite, similar to the dolomite of

235 the bottom detrital level and of the well-preserved part of the massive dolostone level. Bird

236 eyes are filled by a clear sub-planar dolomite with a dark reddish luminescence, while

237 dolomitic cloudy rhombs coating bird eyes have a red luminescence. A small detrital fraction

238 (quartz, feldspar, Fe-Ti oxides, apatite, zircon) is also observed. On top of this level, a

239 dedolomitized limestone (Figs. 3E and F) is observed beneath the unconformity with

240 Pliensbachian arkoses (Fig. 2).

241     At distance from the mineralized zone — ~4 km south of the Aïn Beida fault in the Jbel

242 Bou Moktha — (Fig. 1B), the Sinemurian series display a well-exposed platform margin

243 system with a north-south lateral facies evolution from (1) lagoonal peloidal-oncoidal

244 dolostones to (2) bioclastic/oolitic grainstones (shoal) and finally to (3) marl/limestone

245 alternation (upper slope). This outcrop in the Jbel Bou Moktha allows to precisely locate the

246 bioclastic/oolitic shoal, protecting the lagoon to the open marine environment. At this

247 location, the lateral equivalent of the UCU only displays an early generation of micritic

248 dolomite followed by several calcite cements (Figs. 3G and H).

249   4.1.2 Carbonates phases associated to the ores

250 The three ore-related dolomite phases are not observed outside the mineralized area. Table
251 8 shows the key identification criteria for the dolomite phases.

252 *4.1.2.1 Early diagenetic dolomite phase (Dol-1)*

253 The earliest dolomitic phase (labeled Dol-1a) replaces calcite precursor, here peloids
254 or ooids. Dol-1a is micro-saccharoidal with red color in CL (Figs. 3A and B). Dol-1b
255 precipitates around Dol-1a with a similar luminescence, unzoned in CL (Fig. 3B). Dol-1a and
256 Dol-1b are the most common carbonate phases.

257 *4.1.2.2 Ore-related epigenetic to hydrothermal dolomite phases (Dol-2 and Dol-3)*

258 Coarse grain dolomite phases (Dol-2 and Dol-3) are intimately related to the highly
259 recrystallized part of the massive dolostone and to the mineralization (Figs. 3C). None of
260 these dolomites occur in the unmineralized zone. Dol-2a is a cloudy dolomite related to the
261 dissolution of sedimentary elements in the massive dolostone and forms mostly planar to
262 sub-planar rhombs with size of ~10–20 μm, cloudy in PPL and bright orange, unzoned in CL.
263 Dol-2a is intrinsically associated with another phase (Dol-2b), which is likely related to the
264 alteration of Dol-2a as shown by impregnation of Dol-2b into Dol-2a (Figs. 3C). Dol-2b is a
265 void and vein filling dolomite, much clearer than Dol-2a in PPL, and characterized by well-
266 developed (hundred microns) sub-planar to non-planar rhombs, bright greenish-yellowish
267 zoned in CL. Dol-2b is a blocky cement but is also connected to veinlets (Fig. 3C).

268 The last dolomite phase (Dol-3) is observed as cement and vein- or breccia-filling. Dol-
269 3a replaces Dol-2b and forms either a clear dolomite in PPL and dark in CL, or a dark cloudy
270 dolomite (Fig. 3C), bright red-orange unzoned in CL (Fig. 3F). Dol-3b is a clear sub-planar to
271 non-planar (saddle) coarse (hundred microns) rhomb dolomite. A zoned to unzoned dark
272 reddish luminescence characterizes Dol-3b.

273 *4.1.2.3 Late meteoric calcite phases*

274 Late calcite phases also occur across the whole sedimentary series filling the remaining
275 porosity and cutting-across the host dolostone as mm-sized veins. Two generations of calcite
276 are distinguished. The first one (Cal 1) displays yellowish color in CL with zoned
277 scalenohedron crystals in fractures and as replacement of a former dolomite crystal
278 (dedolomite). The second (Cal 2) postdates Dol-3 and is extinct in CL forming sparitic to
279 anhedral crystals in fractures or in breccia (Fig. 3E and 3F).

280 ***4.2 Ore mineralogy and petrography***

281   Crosscutting relationships and mineral assemblages indicate the presence of two
282 distinct stages of Mn mineralization (Fig. 4). Veins systematically crosscut both the
283 replacement and karst mineralization. Hausmannite and manganite crystals are crossed or
284 replaced by pyrolusite and later by goethite. It suggests the existence of a prior
285 mineralization related to the formation of Mn(II) and Mn(III) oxides and the existence of two
286 Fe oxyhydroxide stages (Gth1 and Gth2).

287 4.2.1. Macroscopic features of the Mn-Fe mineralization

288   From 1922 to 1966, the Bou Arfa manganese deposit was one of the main Mn
289 producers in Morocco with a final production of about ~2 Mt Mn (Mouttaqi et al., 2011). The
290 Mn ore produced metallurgic Mn (33% Mn, 17% Fe) and chemical Mn (82% Mn, <3% Fe;
291 Pouit 1964, 1980; Pouit and Jouravsky 1965; Michard and Raddi 2011; Mouttaqi et al. 2011).
292 The mine remains closed since the seventies. The main mining site is located at Aïn Beida
293 with significant underground works (Figs. 1 and 3). The ore is also well exposed along the
294 Hamaraouet cliff (Figs. 1B and 5A), which constitutes an erosion limit between the basement
295 and the cover; minor mining activities are still in place but galleries in the Upper Chocolate
296 Unit (UCU) are preserved (Figs. 5A and B). From Aïn Beida to Hamaraouet, the Mn
297 mineralization occurs as: (1) a continuous 1-6 meters thick stratabound orebody (~2 km) by
298 replacement of the UCU (Fig. 5C), and (2) veins, stockworks, breccia karst-like (pockets,
299 lenses, cluster) mineralization filling open spaces (Figs. 5D-H; Pouit and Jouravsky 1965;
300 Pouit 1980). This second mineralization is the most important in terms of tonnage and grade.
301 It intensifies toward the core of the Bou Arfa anticline (Fig. 1B) and follows a NE-SW
302 direction parallel to Atlasic directions. It can be subdivided into three sub-groups:

303 (i) The main sub-type is a prismatic karst-like mineralization forming vertical pipes formerly
304   attributed to the "run-type" ore (Pouit and Jouravsky, 1965). This mineralization is ~100
305   m long and corresponds to karst collapse structure composed by dolostone blocks
306   embedded in the Mn-Fe mineralization (pyrolusite, manganite, psilomelane, goethite and
307   hematite) and secondary Mn carbonates (Mn-calcite and rhodochrosite). Their main axis
308   follows an ENE direction. According to Pouit and Jouravsky (1965), veins of various
309   sizes (Figs. 5F and 5G) and Mn stockworks (Fig. 5H) are also connected to this
310   mineralization.

311 (ii) Tabular karst-like mineralization (Fig. 5C) are ten meters long and wide with a thickness
312   of several meters. It follows a sedimentary discontinuous/erosive surface in the upper
313   part of the massive dolostone level of the UCU (Fig. 2) and corresponds to a network of
314   metric channels, parallel to the Sinemurian dolostone strata.

315    (iii) Finally, local veins are described through the Upper Pliensbachian sandstone. Despite
316         the local specificity of this poorly extended mineralization, Pouit and Jouravsky (1965)
317         indicate that it is likely related to a main fault. Impregnation of stratabound pyrolusite is
318         related to this vein (Figs. 5F and 5G).

319 The Bou Arfa mineralization is a mixed Mn-Fe type (25% Mn, 10-12% Fe in the bulk ore)
320 dominantly composed of pyrolusite with manganite in the deeper zone, and locally coronadite
321 group minerals (coronadite, hollandite and cryptomelane). Goethite and hematite are
322 systematically present, sometimes forming massive veins (Fig. 5F). Gangue minerals are Mn
323 carbonates, quartz, calcite and barite (Pouit, 1980).

324 4.2.2 Replacement mineralization

325      The replacement mineralization is mainly composed of pyrolusite (Fig. 5C),
326 crosscutting and replacing Dol-1b or Dol-2 (Fig. 6A). Pyrolusite occurs as elongated cleaved
327 prismatic crystals with bipyramidal sections (Fig. 6B). Several micrometric disoriented
328 needles of pyrolusite filling voids are present at the base of prismatic pyrolusite crystals (Fig.
329 6C), which means at least two generations of pyrolusite. Pyrolusite grows onto sub-planar to
330 non-planar altered crystals of Dol-2b. Dol-3b cements pyrolusite (Fig. 6B).

331      Raman peaks of pyrolusite (Julien et al., 2002, 2004) are identified with a broad shape
332 around $538 \pm 5$ cm$^{-1}$ and $750 \pm 5$ cm$^{-1}$ (Fig. 6D). An additional peak close to $630 \pm 5$ cm$^{-1}$ is
333 also measured. The peak broadening and the presence of an additional peak at $630 \pm 5$ cm$^{-1}$
334 are characteristic of slight deviations of the lattice and especially to de Wolff defects
335 corresponding to additional corner-sharing $[MnO_6]^{8-}$ octahedra (such as in 1×2 tunnel oxide
336 structure; de Wolff 1959; Julien et al. 2002). Other phases are also present in the
337 stratabound orebodies such as colloform Fe oxides (goethite) and some phyllosilicates
338 (smectite or biotite in EDS analyses). Colloform goethite crystals are surrounded by micro-
339 pyrolusite (Fig. 6E).

340   4.2.3 Karst and vein-related mineralization

341      The Hamarouet karst mineralization is mainly composed of Mn oxides and to a lesser
342 extent of Fe oxyhydroxides. Hausmannite forms euhedral crystals crosscut by Dol-3 (Figs.
343 7A and B). Hausmannite is ribbed by cleaved pyrolusite crystals that fill fissures with
344 cryptomelane (7A and B). Hausmannite is replaced by chalcophanite or cryptomelane (Figs.
345 7A and B). The iron mineralization is composed of centimeter rubbed dark goethite (with
346 hematite) crosscut by calcite. This mineralization has a colloform habit and evolves to micro
347 specular at the borders of the Mn ore (Fig. 7E). Fe oxyhydroxides also form a continuous
348 uniform reddish level surrounding lenticular mineralization and are mostly related to the

349   prismatic karst (Fig. 5G). These reddish levels are composed of micro disoriented needles of

350   pyrolusite replacing large Dol-2b rhombs.

351       Colloform early manganite (γ-MnOOH) occurs as planar crystals of ten to a hundred

352   microns (Figs. 7C and D). These crystals form lenticular masses with rare hausmannite and

353   barite crystals (Fig. 7D). Manganite is only observed in Aïn Beida.

354   Carbonate phases are also associated to the Mn-bearing ore minerals and are similar to

355   those observed in the host-rock. Dol-2b, Dol-3 and late calcite phases are observable (Figs.

356   3F, 7A and B). The late stage calcite is also associated with the precipitation of P-rich

357   minerals (apatite) and some phyllosilicates (smectite or biotite; Fig. 3E). Dol-2b crisscrosses

358   manganite-hausmannite phases at Aïn Beida, when Dol-3 fills voids (Fig. 7A) and surrounds

359   hausmannite. In Aïn Beida area a late Ca-rich rhodochrosite, partially replacing manganite

360   and Dol-2b crystals is observable (Fig. 7C and D).

361   4.2.4 Crystallinity of the Fe oxides

362       According to the Scherrer formulation (Langford and Wilson, 1978; Scherrer, 1918), the

363   average size of the crystallite populations of hematite and goethite ranges between 0.02 and

364   0.12 µm in the whole dataset (Fig. 8). These values were measured at the maximum width of

365   each crystal or in the middle of the crystal and are in good agreement with different studies

366   (Cornell and Schwertmann, 2003; Gualtieri and Venturelli, 1999; Rendon et al., 1983;

367   Schwertmann et al., 1985). The crystallite size of hematite in the stockwork mineralization of

368   Bou Arfa is close to a proto-hematite. This type of hematite is a non-stoichiometric phase,

369   which is characteristic of the transformation by dehydration of goethite into hematite beyond

370   140 °C in laboratory experiments (Gualtieri and Venturelli, 1999; Pomiès et al., 1998; Walter

371   et al., 2001; Wolska and Schwertmann, 1989; Wolska and Szajda, 1988). This proto-

372   hematite is not an authigenic phase and possesses two distinct groups of crystallites (Lima-

373   de-Faria, 1963). Schwertmann et al. (1985) have shown that the dimension of the a-cell

374   parameter is a witness of the formation temperature of goethite. A long distance

375   (4.626±0.005A) refers to a low temperature of formation (4–40°C), whereas a shorter

376   dimension (4.610±0.001A) corresponds to higher temperatures (50–90°C). The cell

377   dimensions of four Bou Arfa goethites (Table 9) recovered from the reticular distance of

378   planes (200), (040) and (111) are close to a synthetic goethite crystallized at 50 °C. It is also

379   worth noting that a decrease in the peak intensity of 2.45A is characteristic of goethite

380   formed at >40 °C (Schwertmann et al., 1985), which is actually the case in Bou Arfa goethite

381   (see DR2).

382   ***4.3. Geochemistry***

383 4.3.1 Mineral chemistry

384 *4.3.1.1 Carbonates*

385       EPMA results on dolomite and calcite are reported in Table 4 and plotted in Fig. 9. All
386 the dolomitic phases show excess Ca (26.3 wt.% to 37.8 wt.%; Figs. 9A and B; Table 4). No
387 significant variation is observed to distinguish most of the different generations of dolomites
388 (Figs. 9A and B). Only vein-filling Dol-3 significantly differs from the others, as it contains the
389 highest MnO content (between 1.21 and 9.03 wt.%; Table 4). MnO enrichment implies that
390 late dolomite is close to kutnohorite. It is worth emphasizing that although FeO content (0.13
391 to 1.11 wt.%; Table 4) is lower than MnO, the absolute FeO/MnO ratio is lower than for most
392 of the sedimentary dolomites (Fig. 9C; Searl and Fallick 1990; Montanez and Read 1992;
393 Gasparrinia et al. 2003; Fu et al. 2006). The total amount of trace elements slightly
394 decreases from Dol-1 to Dol-3. The Sr concentration is lower than common marine
395 carbonates (Brand and Veizer, 1980; Zenger et al., 1980). The two late calcite phases are
396 also distinguished, one is Fe-rich, whereas the other is Mn-rich.

397 *4.3.1.2 Manganese oxides*

398       Hausmannite displays minor amounts of $SiO_2$ (0.05 to 0.30 ± 0.01 wt.%), ZnO (0.05 to
399 2.08 ± 0.02 wt.%) and $Fe_2O_3$ (0.55 to 1.55 ± 0.24wt.%). Other elements such as $Na_2O$, MgO,
400 $Al_2O_3$ or SrO are present at very low concentrations. As hausmannite is commonly replaced
401 by chalcophanite (Fig. 6F), some of the EPMA compositions may be affected.

402       The composition of pyrolusite is heterogeneous. All pyrolusite contain substantial
403 amounts of $Al_2O_3$ (5.75 ± 0.03 wt.%), $SiO_2$ (2.11 ± 0.03 wt.%) and CaO (2.25 ± 0.05 wt.%).
404 Only the late-stage pyrolusite grains contain significant amounts of MgO (0.06-1.63 wt.%)
405 and $K_2O$ (0-2.27 wt.%). Pyrolusite in stratabound ores (gallery 63) shows a low CaO content
406 (0.20 ± 0.06%) and the highest $Al_2O_3$ (0.89 ± 1.12 wt.% to 1.30 ± 0.53 wt.%). All the vein-
407 related pyrolusite have a homogeneous composition.

408       EPMA analyzes also reveal that coronadite group minerals – here represented by
409 hollandite and cryptomelane following the nomenclature of Biagioni et al. (2013) –,
410 concentrate Ba, Sr, K, Ca and Mg (Table 5). K, Ba and Mg are the dominant cations and only
411 hollandite is observed as a pure end-member. Chalcophanite sometimes displays very low
412 Zn concentration, instead of Mg, which could be dominant (up to 4.89 wt.%).

413 *4.3.1.3 Goethite and hematite*

414       All analyzed hematite and goethite samples are from Hamaraouet (Fig. 1B). The total
415 $Fe_2O_3$ content is abnormally low for goethite and hematite (Table 6) in comparison with their

416 ideal formula. The total $Mn_2O_3$ and $SiO_2$ contents delimit two geochemical trends: (i) The

417 massive colloform goethite and the Fe oxides associated with dedolomitization are enriched

418 in $Mn_2O_3$ (mean values from 1.46 ± 0.24 to 2.30 ± 0.10 wt.%; Table 6) with minor $SiO_2$ (mean

419 values from 0.11 ± 0.06 to 0.49 ± 0.47 wt.%) and; (ii) The goethite in veins are enriched in

420 $SiO_2$ (mean values from 1.71 ± 0.14 to 3.50 ± 0.4 wt.%) with minor $Mn_2O_3$ content (mean

421 values from 0.09 ± 0.01 to 0.16 ± 0.02 wt.%; Table 6). Goethite and hematite also exhibit

422 minor concentrations of $Al_2O_3$, MgO, CaO, $P_2O_5$ and $K_2O$ (ranging from 0.02 to 0.75 wt. %).

423 4.3.2 Bulk-rock and Mn-ore geochemistry

424 The Sinemurian dolostones display similar geochemical patterns irrespective of the

425 dolomitizing event that affected these rocks (Fig. 10A). The presence of detrital phases such

426 as quartz, feldspars, zircon, monazite and Ti-oxides explains some high immobile and

427 lithophile contents. One of the striking features in all samples is the higher MnO content (0.74

428 to 4.71 wt.%) comparative to FeO (0.26% to 1.44 wt.%; Fig. 10A; Table 2). The enrichment in

429 As is also significant.

430 The karst Mn ores of Aïn Beida, the stratabound Mn and Fe orebodies and the fracture-

431 filling Fe-Mn mineralization show a similar geochemical signature despite their different

432 mineralogy (Figs. 10A and B). Geochemical patterns are close to those of the host rock but

433 with relatively higher enrichments. Lithophile (V), chalcophile (Pb, Zn, Cu) and siderophile

434 (Co, Ni, Mn) elements are more enriched than in the host rock (Fig. 10A). Ba, As, Zn and Fe

435 contents differ between samples: higher Ba and As contents are recorded at Aïn Beida. The

436 Mn/Fe ratio of samples from Aïn Beida ($Mn/Fe_{AB1}$ = 66.9; $Mn/Fe_{AB2}$ = 1.3, Table 3) is also one

437 of the lowest. The late supergene weathered ores are enriched in Sr (1316 to 2350 ppm), Zn

438 (1446 to 2136 ppm) and $K_2O$ (0.66 to 0.96 wt.%), likely due to the presence of hollandite,

439 cryptomelane and chalcophanite. Concentration in lithophile, immobile elements and in REE

440 are low compared to the host rock (Fig. 10A).

441 The enrichments of the Fe-rich ores are roughly the same as for the Mn ore with some

442 increase in V, As and Pb in the vein-related hematite of Hamaraouet (Fig. 10B). This

443 mineralization is also enriched in Be (6 to 114 ppm) and Ge (2 to 124 ppm). The Fe ore has

444 also a high Mn content up to 0.14-1.07 wt.% $Fe_2O_{3t}$ (Table 3).

445 Overall, As and Mn are enriched in both the host dolostone and in the mineralization

446 (Tables 2 and 3). Paleozoic schists are depleted in Mn (0.02 wt.% MnO). Chalcophile

447 elements (As, Pb, Zn, Cu) are abundant in the Mn ores and in most of the Fe ores (Fig. 10A

448 and B; Table 3).

449 4.3.3 Carbon and oxygen isotopic compositions of carbonates

14

450    The analyzed carbonates show a wide range of carbon and oxygen isotopic

451    compositions with $\delta^{13}C_{VPDB}$ and $\delta^{18}O_{VSMOW}$ ratios ranging from -8.6 to 2.2‰ and 17.3 to

452    29.8‰, respectively (Fig. 11; Table 7). $\delta^{18}O_{VSMOW}$ and $\delta^{13}C_{PDB}$ ratios for the primary Dol-1

453    phase are rather homogenous clustering around 29.2‰ and 29.8‰ for $\delta^{18}O_{VSMOW}$ and 0.1‰

454    to 2.2‰ for $\delta^{13}C_{VPDB}$. Later dolomite phases (Dol-2 and Dol-3) display $\delta^{18}O$ values from

455    17.3‰ to 28.6‰ VSMOW and $\delta^{13}C$ values ranging from -7.8‰ to 2.1‰ VPDB. Based on

456    $\delta^{13}C$ values, there is a slight distinction between the Dol-2 cement in the host rock (average

457    value: -0.04 ± 0.40‰ VPDB) and the heavier $\delta^{13}C$ values of the vein filling Dol-2 (mainly

458    represented by Dol-2b; average value: 1.01 ± 0.95‰ VPDB; Fig. 11). Vein-filling Dol-3 shows

459    the lightest $\delta^{13}C$ values (Fig. 11). Some values are heavier, but this may likely be due to

460    impurities in Dol-2 during the analysis. For Dol-2 and Dol-3, both $\delta^{13}C$ and $\delta^{18}O$ values

461    evolve simultaneously towards lighter isotopic values. Late calcite cements display values

462    ranging from 19.5 to 23.1‰ for $\delta^{18}O$ and from -8.5 to -6.1‰ for $\delta^{13}C$ (Fig. 11).

463    **5. DISCUSSION**

464    *5.1. Paragenetic sequence*

465    The formation of the Mn(-Fe) ores of Bou Arfa can be summarized in three main

466    stages: (i) Mn-Fe protore, (ii) main Mn-Fe ore and (iii) post ore (Fig. 4). The second stage is

467    economically the most important accounting for most of the extracted Mn ore in the Bou Arfa

468    district, which is mainly expressed by the occurrence of massive pyrolusite. The multistage

469    deposition of Mn-bearing minerals was accompanied by several dolomitization synchronous

470    with the first two stages of Mn deposition (Fig. 4).

471    5.1.1 Mn-Fe protore

472    Manganite and hausmannite (Figs. 6F, 7A, B, C) accompany Dol-2, along with colloform to

473    specular Mn-rich Fe oxyhydroxides (goethite and hematite) and barite (Fig. 4). This early

474    Mn(-Fe) mineralization is mainly observed in the Aïn Beida site (Fig. 1B), but the occurrence

475    of hausmannite in the Hamaraouet area also indicates that early stage of mineralization has

476    a larger extension.

477    5.1.2 Main Mn ore

478    Fracture-filling and karst mineralization are later than Dol-2. Pyrolusite is the only Mn oxide

479    (Figs. 3E, 6A, B, F, G and H) and occurs alongside Si-rich goethite, hematite and Mn-

480    dolomite to Ca-rhodochrosite (Fig. 4). The massive pyrolusite shows a wide range of textures

481    from tiny micrometric needles to large prismatic millimetric crystals (Figs. 3E, 6B and F).

482    Variation of pyrolusite bonds in Raman spectra (Fig. 6D) are interpreted as replacement of

483    manganite (Gaudefroy, 1960; Hewett, 1972; Pasero, 2005; Post, 1999; Yoshino et al., 1993,

484    1992). Prismatic pyrolusite is frequently related to manganite replacement (Fleischer et al.,

485    1962). The replacement of $Mn^{2+}$- or $Mn^{3+}$-bearing minerals by pyrolusite enhances the Jahn

486    Teller deformation pattern by including a c-axis elongated $Mn^{3+}$-octahedra in the pyrolusite

487    structure (Julien et al., 2004; Post, 1999; Post et al., 2003; Zwicker et al., 1962). These

488    textures indicate that this mineralization stage impregnates the host rock dolostone and

489    support that pyrolusite partly replaced manganite. Also important is that pyrolusite remains

490    stable and does not accommodate any supplementary cation other than Mn in its structure,

491    unlike manganite, for which substitutions are facilitated by its layer structure (Post, 1999;

492    Post et al., 2003). Conversion from manganite to pyrolusite explains Si, Al and Ca (>2 wt.%)

493    enrichment in pyrolusite (Tables 3 and 5). Mn-Fe oxides precipitated from a similar

494    mineralizing fluid, although Si-rich Fe oxides formed later than pyrolusite (Fig. 7E). This

495    means that this second ore formation stage partly reworks the early mineralization episode.

496    Although, pyrolusite by replacement of manganite is well documented in the Bou Arfa ore,

497    the main ore consists of open-space filling of pyrolusite (Figs. 6A and F). Botryoidal-hematite,

498    proto-hematite and goethite formed later than Dol-2 and destabilized some dolomitic phases

499    (Fig. 4).

5.1.3 Late stage supergene enrichment

501    The post-ore supergene stage is poorly expressed in the Bou Arfa ores (Fig. 4). This

502    feature is due to the stability of the main ore-forming minerals under surface or near-surface

503    conditions (Post, 1999), such as pyrolusite and Fe oxides. Some typical supergene minerals

504    have unevenly precipitated as chalcophanite or hollandite-cryptomelane (Figs. 6F, 7A and B)

505    in partial replacement of hausmannite. Chalcophanite is a common weathering product in Mn

506    and Zn deposits (Decrée et al., 2010, 2008; Ostwald, 1992; Post, 1999), and its relation with

507    hausmannite is due to little amounts of Zn (0.3 wt.%; Table 5). Pyrolusite is also partially

508    destabilized and transformed into coronadite group minerals (here hollandite and

509    cryptomelane) as it is often the case in the weathering zone of Mn deposits (Ostwald, 1992;

510    Varentsov, 1996). Late calcite cement (Figs. 3E and F) is also associated with the Mn

511    supergene assemblage and extensively develops in the host rock and mineralization (Fig. 4).

512    The meteoric origin of calcite is supported by partial dedolomitisation (Fig. 3E; Ayora et al.

513    1998; Dewaide et al. 2014) and light isotopic values (Fig. 11).

### *5.2 Metallogenic model*

515    5.2.1 Metal source(s) in seawater

516    All mineralization, whatever their stage, display similar geochemical patterns (Fig.
517    10B), close to the signal of the host rock dolostone (Figs. 10A and B). It implies that the three
518    ore stages have a similar origin and that the later stages rework an early stock. Chalcophile
519    (As, Zn, Pb, Cu, Ni, Co, V) and some mobile elements (Sr, Ba, Be; Table 3; Figs. 10A and B)
520    are particularly enriched in the orebodies. However, a Principal Component Analysis (PCA)
521    also links As, V, Mo, Co, Ni, Ba, Zn, Sr, Pb, U to the Mn orebodies, unlike immobile and
522    lithophile, which characterize the host Sinemurian dolostone and the Pliensbachian arkoses
523    (Fig. 12A). This indicates that the Mn ore involves external inputs of Mn and associated
524    metals, i.e. from basement rocks. Therefore, it is likely that upward (hot?) mineralizing fluids
525    additionally participated to the ore formation, for example by mixing with shallower
526    oxygenated ground waters, which might explain the karst-like mineralization (Varentsov,
527    1996). This is materialized in Nicholson's diagnostic plots by a clear hydrothermal trend of
528    the Bou Arfa ores (Figs. 12B; Fig. 12C). In addition, this highlights the difference between the
529    Bou Arfa Mn ores from other carbonate-hosted Mn deposits in Morocco (Fig. 12C; Gutzmer
530    et al. 2006; Dekoninck et al. 2016b, a, 2020).

531    5.2.2 Syn-sedimentary and early diagenetic (pre)concentration

532    The occurrence of evaporitic levels, pisoids, oncoids, bird eyes and micro-saccharoïdal
533    dolomite (Dol-1; Fig. 3) supports a restricted lagoonal environment, part of the platform
534    interior. This restricted lagoon is protected from open marine environments by an ooid and
535    bioclatic sand shoal, probably forming the platform margin 4-5 km south of the Mn ore
536    deposit of Aïn Beida, in the Jbel Bou Mokhta (Fig. 1B). These restricted lagoonal
537    environments are particularly suitable for early dolomitization (Fig. 4; Land 1985; Jones and
538    Renaut 1994; Machel 2004; Arenas-Abad et al. 2010). The oxygen composition of Dol-1 are
539    higher than most common lagoonal dolomite (Blaise et al., 2014; Brigaud et al., 2018;
540    Mauger and Compton, 2011; Ren and Jones, 2017), but they are consistent with shallow
541    depth Mn-rich dolomite (Burns and Baker 1987; Fig. 11). Dolomite (Dol-1) is less abundant in
542    shoal and upper slope facies outside the Bou Arfa (Jbel Bou Moktha; Figs. 1B, 3G and H).

543    In these shallow marine to lagoonal environments, anoxic to suboxic basins or microbial
544    activity are the most suitable trap for Mn (Folk and Chafetz, 2000; Jones and Renaut, 1994;
545    Mandernack et al., 1995b, 1995a; Ostwald, 1990). Microbial activity is usually observed
546    through the coalescence of Mn-Fe-rich pisoid laminae in sedimentary Mn deposits (Groote
547    Eylandt, Chinese, Brazil deposits; Force and Cannon 1988; Frakes and Bolton 1992;
548    Ostwald 1992; Fan and Yang 1999; Fan et al. 1999; Biondi et al. 2020). The absence of Mn-
549    rich or Fe-rich laminae and $\delta^{13}C$ isotopic values of Dol-1 greater than 0‰ VPDB (Fig. 11) are
550    not consistent with Mn and Fe enrichment by bacteria-mediated organic matter degradation

17

551　(i.e., black shales; Okita et al. 1988; Polgári et al. 1991, 2012; Fan et al. 1999; Maynard

552　2014; Johnson et al. 2016). Alternatively, the C-O evolutionary trend shown in Figure 11

553　could be interpreted as resulting from fluid mixing between deep upward migrating warm

554　basinal brines and downward infiltration of later cooler meteoric fluid. However, C-rich layers

555　(i.e., coal, lignite) are not present in the sedimentary series. A second dolomitization episode

556　is recorded by Dol-2, although no textural argument clearly establishes if this second event

557　belongs to an early diagenesis or epigenesis (Fig. 5).

558　　　　The high Mn contents of Dol-1 (up to 1.58 ± 0.51 wt.% MnO in Dol-1; Table 4) suggests

559　an early Mn enrichment (Fig. 9C) under suboxic conditions with the absence Fe sulfides or

560　Fe carbonates (Maynard 2014). Without any contribution of organic matter in the Mn fixation,

561　an extremely high alkaline and anoxic to dysoxic environment (0-0.4 Eh) would prevail.

562　Anoxic-suboxic events related to the closure of a narrow and shallow Bou Arfa basin (Piqué

563　et al., 2000; Yelles-Chaouche et al., 2001) may trap the dissolved $Mn^{2+}$ in pore waters. The

564　porosity increased thanks to the early dolomitization and transformation of the earliest

565　carbonates into dolomite. The high Mg:Mn ratio favors precipitation of dolomite with little

566　amounts of Mn, the major part staying in the pore fluid (Table 2). Burial of the Sinemurian

567　sediments would reinforce suboxic conditions that precipitate $Mn^{2+}$ from pore waters into

568　"reduced" Mn oxides ($Mn^{2+}$ and $Mn^{3+}$), when alkaline conditions are maintained. The high As

569　content in goethite (Table 6) is also consistent with a precipitation under alkaline and suboxic

570　conditions (Campbell and Nordstrom, 2014; Pierce and Moore, 1982). At the same time,

571　dolomitization continued, increasing the porosity of the host rock, and helped to

572　accommodate $CO_3^{2-}$ from pore waters into dolomite phase. The extensive pseudomorphosis

573　between dolomite generations during the ore formation (Figs. 3 and 4) may have limited

574　massive release of $CO_3^{2-}$ in pore waters, and have prevented the formation of Mn-rich

575　carbonates (i.e., Ca-rhodochrosite or kutnohorite; Fig. 4). Only alteration of this primary ore

576　assemblage led to Ca-rhodochrosite (Figs. 4 and 7C; Maynard 2014; Manceau et al. 2014).

577　Consequently, hausmannite and manganite precipitated instead of Mn carbonates. The

578　presence of Mn-rich Fe oxides in the primary stage also indicates a local separation of Fe

579　from Mn at macro/microscopic scale. However, the high Mn content in goethite shows that

580　Fe and Mn probably came with the same mineralizing fluid, but have precipitated separate

581　phases, in different proportions. It likely suggests that the mineralizing fluids carried Mn and

582　Fe with a very low Fe/Mn ratio (Table 6; Fig. 9C).

583　5.2.3 Late diagenetic evolution and hydrothermal circulation during burial

584　　　　The synchronous precipitation of manganite, hausmannite and barite in Mn deposits

585　are commonly attributed to thermal conditions with temperatures much higher (250-350°C)

than at the surface (Fan et al., 1999; Gutzmer and Beukes, 1996; Hewett, 1972). Dol-2b and Dol-3 display sub-planar to saddle texture (Figs. 3C and F) due to an increase of temperature (Blaise et al., 2014; Radke and Mathis, 1980; Searl, 1989). Decrease of the $\delta^{18}O$ values and slight decrease of $\delta^{13}C$ values from Dol-1 to Dol-2 (Fig. 9) is characteristic of an isotopic re-equilibration triggered by a temperature increase (Brand and Veizer, 1981; Lee and Friedman, 1987; Nader et al., 2007, 2006; Warren, 2000). Moreover, $\delta^{18}O$ and $\delta^{13}C$ values of the saddle dolomite (Dol-3) are among the lightest (Fig. 9) and support a continuous increase in temperature along the formation of the dolomite generations, and consequently along the formation of the Bou Arfa Mn(-Fe) ores. The saddle dolomite (Dol-3b) originates from a thermal effect instead of oversaturation of Mg (Searl, 1989; Warren, 2000). The temperature allowing non-planar dolomite (Dol-2b) is close to 50°C and a temperature of 60°C to 80°C is needed for the saddle dolomite formation (Dol-3b; Radke and Mathis 1980; Machel 2000; Warren 2000). This thermal effect is also shown through the crystallography of Fe oxides (Fig. 8; Table 9). In experiments, the formation of proto-hematite occurs beyond ~140°C (Wolska and Schwertmann, 1989) and the short a axis of the goethite cell at Bou Arfa (Table 9) testifies to the higher formation temperatures (>50°C; Schwertmann et al. 1985). This interpretation is further supported by the evolutionary trend shown by the distribution of C and O isotopic data (Fig. 11) and an important change in $\delta^{13}C$ from the classical burial diagenesis in Dol 3. This involves warm basinal brines and their subsequent mixing with downward percolating cooler meteoric fluids. The E-W-trending Aïn Beida fault zone would have enhanced the widespread infiltration of meteoric fluids. These observations indicate that burial and additional hot fluids are the driver for late dolomitization (Dol-2 and Dol-3) and Fe oxide stages (Fig. 5). It is materialized by karst and vein mineralization (Fig. 6A, F, 6A, B and C) and by mineralogical transformations of the primary ore (Fig. 5). The successive dolomite generations are similar to the burial model of Cu-Co deposits described in the Central Africa Copper Belt (Dewaele et al., 2006; El Desouky et al., 2009; Hoy and Ohmoto, 1989). The formation of Mn-rich dolomite and Ca-rhodochrosite are also indicators of burial diagenesis in the Bou Arfa deposit (Fig. 4). Actually, the reductive conditions related to burial and the loss of oxygen renewal is suitable for the partial manganite degradation into Ca-rhodochrosite (Fig. 7C; Roy 2006; Johnson et al. 2016).

Consequently, the genesis of the remobilized ore (Fig. 5) might be due to (i) remobilization of the primary ore and (ii) migration of Mn by diagenetically-driven hydrothermal fluids. The Aïn Beida fault (Fig. 1B) played an important role by facilitating fracturation of the host rock and enhancing Mn-bearing fluid circulation. It is not excluded that hausmannite and manganite resulted from the transformation of former Mn oxides. Such mineral evolution is common in hypogene and metamorphic Mn deposits (Hewett 1972;

622 Nicholson 1992; Gutzmer et al. 1995; Post 1999). There are few petrographical arguments
623 pleading for the presence of an early Mn carbonate precursor as formerly presented by Pouit
624 and Jouravsky (1965).

625 5.2.4. The Cenozoic Atlas exhumation: supergene enrichment

626       Hollandite, cryptomelane and chalcophanite (Figs. 6F and G) were accompanied by
627 dedolomitisation (Fig. 4E). These late meteoric fluids have not substantially enriched the Bou
628 Arfa ore, except maybe for Zn that was concentrated in chalcophanite, and Sr in hollandite-
629 cryptomelane (Table 3). The supergene origin of the Fe oxides is unlikely with their
630 crystallographic features (Fig. 8; Table 9) and explains why these minerals have precipitated
631 later than manganite, hausmannite and pyrolusite. This relatively poor weathering is quite
632 contrasting with the numerous Cu-Zn-Pb-V hypogene deposits of the eastern High Atlas and
633 Anti-Atlas, where an oxidation zone systematically occurs (Bouabdellah et al., 2012; Choulet
634 et al., 2014; Poot et al., 2020; Rddad and Bouhlel, 2016; Verhaert et al., 2018, 2017). The
635 weathering phase recorded in the Bou Arfa ores is probably connected to the repeated
636 exhumation of the Atlas since late Cretaceous times (Dekoninck et al., 2020; Frizon de
637 Lamotte et al., 2000; Froitzheim, 1984; Leprêtre et al., 2018, 2015).

638 *5.3 Place of the Mn Bou Arfa deposit in the Mesozoic evolution of the Atlas*

639 Without geochronological constraints, the absolute timing of the Bou Arfa Mn(-Fe)
640 mineralization is difficult to establish, but has seemingly occurred after the deposition of the
641 Sinemurian carbonates. Sinemurian dolostones were deposited in the context of rifting and
642 deepening of several sedimentary basins along the Atlas belt (Frizon de Lamotte et al., 2009;
643 Nottvedt et al., 1995; Teixell et al., 2009; White and McKenzie, 1988). This setting would
644 explain the position of the Bou Arfa Mn deposit, as the basin could act as a threshold, given
645 its location above a paleohigh. The strong variation in the thickness of the sedimentary series
646 in the Bou Arfa basin indicates an important variation of the geometry and/or significant
647 lateral variation of the sedimentary facies that would have delimited the extension of the Mn
648 mineralization (Torres-Ruiz, 1983). This sharp transition of sedimentary facies is well
649 demonstrated in the Jbel Bou Moktha (Fig. 1B), where the Sinemurian carbonate facies
650 evolves from a lagoonal (dolomitic-peloidal facies) to an offshore environment
651 (marls/limestones alternations). Transgression events during the Sinemurian interval
652 repeatedly supplied dissolved $Mn^{2+}$, and when the Bou Arfa area was isolated from seawater
653 influxes, was trapped in pore waters. The situation of the Bou Arfa deposit in a narrow basin
654 pinched to the north by the Tendrara rift shoulder and to the south by a narrow ditch (Tamlet
655 plain; Piqué et al. 2000; Yelles-Chaouche et al. 2001) was an efficient trap for dolomitization
656 and Mn pre-concentration. The position of the deposit above paleohigh basement rocks and

657    close to a major tectonic thrust (Fig. 1B) have provided suitable conditions for brecciation

658    and fracking enhancing diagenetically-driven hydrothermal circulation in porous Sinemurian

659    dolostones.

660    The metallogenesis of the Bou Arfa ores is different from the high-grade Imini-Tasdremt Mn

661    deposits (Figs. 12B and C). Accordingly, the Imini-Tasdremt Mn ores postdate the latest

662    meteoric dolomite generation and do not show any Mn precursor (Dekoninck et al., 2016a)

663    nor saddle dolomite (Force et al., 1986). Moreover, the host dolostone is intensely karstified

664    with dissolution and collapse breccia filled by sands (Gutzmer et al., 2006) and the age of the

665    Mn ore span over a period of ~25 Ma during the late Cretaceous (Dekoninck et al., 2020).

666    The accepted formation model of the Imini-Tasdremt ores involves mixing of $O_2$-rich meteoric

667    waters and acidic $O_2$-free ground waters (Gutzmer et al., 2006). For these reasons, the

668    comparison between these two carbonate-hosted Mn deposits is unfaithful although the

669    dolomitic trap has some similarities, i.e. the isotopic composition (Fig. 11) and Fe:Mn ratios

670    (Fig. 9C) of the host dolostones.

671    **5.4. Relation of the Bou Arfa Mn(-Fe) ores with Mississippi Valley Type deposits in**

672    **North Africa**

673    Mississippi Valley Type (MVT) deposits are widespread along Meso-Cenozoic shallow-water

674    carbonate platforms forming the Atlas system (Bouabdellah and Sangster, 2016; Decrée et

675    al., 2016). The occurrence of numerous Pb-Zn MVT and Cu mineralization in Jurassic series

676    of the Bou Arfa region (Fig. 1; e.g., Chefchaouni et al. 1963; Verhaert et al. 2017, 2018) also

677    supports the predominant role of dolostone in trapping various metals. The Bou Arfa deposit

678    is comparable with major Zn-Pb MVT deposits of Morocco (Bouabdellah et al., 2015, 2012;

679    Bouabdellah and Sangster, 2016; Jébrak et al., 1998; Rddad, 2021; Rddad et al., 2018;

680    Rddad and Bouhlel, 2016) at several levels: (1) they are hosted in Lower to Middle Jurassic

681    unmetamorphosed platform carbonate rocks; (2) the mineralization fills open spaces (veins,

682    interconnected cavities, solution-collapse breccias) and replaces carbonate; (3) the

683    mineralization is accompanied by different generations of saddle dolomite or calcite; (4) the

684    deposits are located above basement paleohighs where Triassic to Jurassic rocks are

685    pinched out; and (5) the ENE-WSW and E-W faults have facilitated fluid circulation in

686    permeable rocks hosting the ore. The genesis of Pb-Zn MVT mineralization in Morocco is

687    explained by ascending diagenetically-derived hydrothermal solutions due to compaction

688    and/or gravity-driven systems mixing with surficial cooler fluids. The mineralizing fluids were

689    forced to spread laterally along the porous Lower and Middle Jurassic aquifer due to Upper

690    Jurassic cap rock (Bouabdellah and Sangster, 2016). MVT deposits are likely formed before

691    the onset of the non-sulphide supergene ores supposed at ~20 Ma (Choulet et al., 2014;

21

692 Verhaert et al., 2017). The heat source for MVT deposits in the Atlas range may derived from
693 the Alpine orogenesis itself that caused large-scale fluid circulation of deep-seated fluids
694 rather than direct volcanic activities (Rddad, 2021). The High Atlas has indeed a thin
695 lithosphere supported by a thermal anomaly since the Miocene (Leprêtre et al., 2018 and
696 reference therein), which has provided proper thermal conditions for various mineralization
697 types in the High Atlas. Such interpretation can be applied to the Bou Arfa Mn(-Fe) deposit.

698 **6. CONCLUSIONS**

699 This study emphasizes the role of dolomitization in the formation of the Bou Arfa Mn(-
700 Fe) deposit. The accumulation of the Bou Arfa Mn ores follows a multistage genesis in close
701 association with three dolomite events. Early diagenesis (Dol-1 and Dol-2) and epigenesis
702 (Dol-3) are associated with the mineralization process by providing suitable conditions for Mn
703 oxides precipitation instead of Mn carbonates. The porosity, depletion in dissolved carbonate
704 species in pore waters and suboxic conditions are responsible for the primary hausmannite,
705 manganite, barite and (Mn-)goethite assemblage. The subsequent burial of the host
706 Sinemurian dolostone is clearly observed through (i) a textural evolution from non-planar
707 (Dol-2b) to saddle dolomite (Dol-3), (ii) a decrease in the $\delta^{13}C$ and $\delta^{18}O$ isotopic values and
708 (iii) crystallographic changes of the Fe oxides. This increase in temperature and pressure
709 triggered mineralogical transformations of the primary manganite into massive pyrolusite with
710 (Si-)goethite, hematite and (Mn-)dolomite to Ca-rhodochrosite, whereas hausmannite
711 remained stable. Diagenetically-driven hydrothermal circulation, enhanced by the vicinity of
712 the Aïn Beida fault, is responsible for the formation of deep karst and vein-type Mn and then
713 Fe ores. A mixing fluid model is also suitable for the late evolution of the Mn mineralization. It
714 emphasizes that goethite and some of the Mn oxides, commonly attributed to strictly
715 supergene conditions, were formed under higher temperatures (>50°C). The supergene
716 contribution is very low given the stability of the ore-forming minerals under supergene
717 conditions. Weathering only proceeded through partial replacement of hausmannite (and
718 rarely pyrolusite) into chalcophanite and coronadite group minerals.

719 The Bou Arfa deposit can be considered as a diagenetic deposit showing similarities
720 with MVT deposits of North Africa, where a predominant role is played by dolomitization. In
721 the context of global extension (opening of Tethys) forming several Jurassic basins along the
722 High Atlas, the Bou Arfa area played differently due to local settings. This narrow basin lying
723 above a paleohigh basement in a heavily faulted zone probably facilitated circulation of
724 diagenetic fluids and strictly delimited the geometry of the Mn ores. Transgression-regression
725 intervals determined the input of dissolved Mn into the basin.

726 **Acknowledgement**

734    **References**

735    Arenas-Abad, C., Vázquez-Urbez, M., Pardo-Tirapu, G., Sancho-Marcén, C., 2010. Chapter
736         3 Fluvial and Associated Carbonate Deposits, in: Developments in Sedimentology.
737         Elsevier, pp. 133–175. https://doi.org/10.1016/S0070-4571(09)06103-2

738    Ayora, C., Taberner, C., Saaltink, M.W., Carrera, J., 1998. The genesis of dedolomites: a
739         discusion based on reactive transport modeling. Journal of Hydrology 209, 346–365.
740         https://doi.org/10.1016/S0022-1694(98)00095-X

741    Biondi, J.C., Polgári, M., Gyollai, I., Fintor, K., Kovács, I., Fekete, J., Mojzsis, S.J., 2020.
742         Biogenesis of the Neoproterozoic kremydilite manganese ores from Urucum (Brazil) –
743         A new manganese ore type. Precambrian Research 340, 105624.
744         https://doi.org/10.1016/j.precamres.2020.105624

745    Blaise, T., Barbarand, J., Kars, M., Ploquin, F., Aubourg, C., Brigaud, B., Cathelineau, M., El
746         Albani, A., Gautheron, C., Izart, A., Janots, D., Michels, R., Pagel, M., Pozzi, J.-P.,
747         Boiron, M.-C., Landrein, P., 2014. Reconstruction of low temperature (<100 °C) burial
748         in sedimentary basins: A comparison of geothermometer in the intracontinental Paris
749         Basin. Marine and Petroleum Geology 53, 71–87.
750         https://doi.org/10.1016/j.marpetgeo.2013.08.019

751    Bouabdellah, M., Niedermann, S., Velasco, F., 2015. The Touissit-Bou Beker Mississippi
752         Valley-Type District of Northeastern Morocco: Relationships to the Messinian Salinity
753         Crisis, Late Neogene-Quaternary Alkaline Magmatism, and Buoyancy-Driven Fluid
754         Convection. Economic Geology 110, 1455–1484.
755         https://doi.org/10.2113/econgeo.110.6.1455

756    Bouabdellah, M., Sangster, D.F., 2016. Geology, Geochemistry, and Current Genetic Models
757         for Major Mississippi Valley-Type Pb–Zn Deposits of Morocco, in: Bouabdellah, M.,
758         Slack, J.F. (Eds.), Mineral Deposits of North Africa, Mineral Resource Reviews.
759         Springer International Publishing, Cham, pp. 463–495. https://doi.org/10.1007/978-3-
760         319-31733-5_19

761    Bouabdellah, M., Sangster, D.F., Leach, D.L., Brown, A.C., Johnson, C.A., Emsbo, P., 2012.
762         Genesis of the Touissit-Bou Beker Mississippi Valley-Type District (Morocco-Algeria)
763         and Its Relationship to the Africa-Europe Collision. Economic Geology 107, 117–146.
764         https://doi.org/10.2113/econgeo.107.1.117

765    Brand, J., Veizer, J., 1980. Chemical diagenesis of a multicomponent carbonate system:
766         trace elements. SEPM Journal of Sedimentary Research Vol. 50.
767         https://doi.org/10.1306/212F7BB7-2B24-11D7-8648000102C1865D

768    Brand, U., Veizer, J., 1981. Chemical diagenesis of a multicomponent carbonate system; 2,
769         Stable isotopes. Journal of Sedimentary Research 51, 987–997.
770         https://doi.org/10.1306/212F7DF6-2B24-11D7-8648000102C1865D

771    Brigaud, B., Vincent, B., Pagel, M., Gras, A., Noret, A., Landrein, P., Huret, E., 2018.
772         Sedimentary architecture, depositional facies and diagenetic response to intracratonic
773         deformation and climate change inferred from outcrops for a pivotal period
774         (Jurassic/Cretaceous boundary, Paris Basin, France). Sedimentary Geology 373, 48–
775         76. https://doi.org/10.1016/j.sedgeo.2018.04.011

776  Burns, S.J., Baker, P.A., 1987. A geochemical study of dolomite in the Monterey Formation,
777      California. Journal of Sedimentary Research 57, 128–139.
778      https://doi.org/10.1306/212F8AC6-2B24-11D7-8648000102C1865D
779  Calvert, S.E., Pedersen, T.F., 1996. Sedimentary geochemistry of manganese; implications
780      for the environment of formation of manganiferous black shales. Economic Geology
781      91, 36–47. https://doi.org/10.2113/gsecongeo.91.1.36
782  Campbell, K.M., Nordstrom, D.K., 2014. Arsenic Speciation and Sorption in Natural
783      Environments. Reviews in Mineralogy and Geochemistry 79, 185–216.
784      https://doi.org/10.2138/rmg.2014.79.3
785  Cannon, W.F., Force, E.R., 1983. Potential for high-grade shallow-marine manganese
786      deposits in North America, in: Cameron Volume on Unconventional Mineral Deposits.
787      American Institute of Mining, Metallurgical and Petroleum Engineers, New York, NY,
788      pp. 175–189.
789  Chefchaouni, Y.C., Diouri, M., Choubert, G., 1963. Carte géologique de la France à 1/50
790      000, 341, Gérardmer. Notes et mémoires du Service géologique du Maroc.
791  Choubert, G., Faure-Muret, A., 1973. The Precambrian iron and manganese deposits of the
792      Anti-Atlas, in: Genesis of Precambrian Iron and Manganese Deposits. Presented at
793      the Unesco Earth Sciences Symposium, Kiev, pp. 115–124.
794  Choubert, G., Faure-Muret, A., 1962. Evolution du domaine atlasique marocain depuis les
795      temps paléozoïques, in: Livre à La Mémoire Du Professeur Paul Fallot, Mémoire Hors
796      Série. Société Géologique de France, Paris, pp. 447–527.
797  Choulet, F., Charles, N., Barbanson, L., Branquet, Y., Sizaret, S., Ennaciri, A., Badra, L.,
798      Chen, Y., 2014. Non-sulfide zinc deposits of the Moroccan High Atlas: Multi-scale
799      characterization and origin. Ore Geology Reviews 56, 115–140.
800      https://doi.org/10.1016/j.oregeorev.2013.08.015
801  Cornell, R.M., Schwertmann, U., 2003. The Iron Oxides: Structure, Properties, Reactions,
802      Occurences and Uses, 1st ed. Wiley. https://doi.org/10.1002/3527602097
803  de Wolff, P.M.D., 1959. Interpretation of some γ-MnO2 diffraction patterns. Acta
804      Crystallographica 12, 341–345. https://doi.org/10.1107/S0365110X59001001
805  Decrée, S., De Putter, T., Yans, J., Moussi, B., Recourt, P., Jamoussi, F., Bruyère, D.,
806      Dupuis, C., 2008. Iron mineralisation in Mio-Pliocene sediments of the Tamra iron
807      mine (Nefza mining district, Tunisia): Mixed influence of pedogenesis and
808      hydrothermal alteration. Ore Geology Reviews 33, 397–410.
809      https://doi.org/10.1016/j.oregeorev.2007.02.001
810  Decrée, S., Marignac, C., Abidi, R., Jemmali, N., Deloule, E., Souissi, F., 2016.
811      Tectonomagmatic Context of Sedex Pb–Zn and Polymetallic Ore Deposits of the
812      Nappe Zone Northern Tunisia, and Comparisons with MVT Deposits in the Region, in:
813      Bouabdellah, M., Slack, J.F. (Eds.), Mineral Deposits of North Africa. Springer
814      International Publishing, Cham, pp. 497–525. https://doi.org/10.1007/978-3-319-
815      31733-5_20
816  Decrée, S., Ruffet, G., Putter, T.D., Baele, J.-M., Recourt, P., Jamoussi, F., Yans, J., 2010.
817      Mn oxides as efficient traps for metal pollutants in a polyphase low-temperature
818      Pliocene environment: A case study in the Tamra iron mine, Nefza mining district,
819      Tunisia. Journal of African Earth Sciences 57, 249–261.
820      https://doi.org/10.1016/j.jafrearsci.2009.08.005
821  Dekoninck, A., Bernard, A., Barbarand, J., Saint-Bezar, B., Missenard, Y., Lepretre, R.,
822      Saddiqi, O., Yans, J., 2016a. Detailed mineralogy and petrology of manganese
823      oxyhydroxide deposits of the Imini district (Morocco). Mineralium Deposita 51, 13–23.
824      https://doi.org/10.1007/s00126-015-0590-3
825  Dekoninck, A., Leprêtre, R., Saddiqi, O., Barbarand, J., Yans, J., 2016b. The high-grade
826      Imini manganese district—karst-hosted deposits of mn oxides and oxyhydroxides, in:
827      Bouabdellah, M., Slack, J.F. (Eds.), Mineral Deposits of North Africa. Springer
828      International Publishing, Cham, pp. 575–594.
829  Dekoninck, A., Ruffet, G., Missenard, Y., Parizot, O., Magoua, M., Mouttaqi, A., Rochez,
830      Gaëtan, Yans, J., 2020. Multistage genesis of the late Cretaceous manganese karst-

831             hosted Tasdremt deposit (High Atlas, Morocco). Mineralium Deposita.
832             https://doi.org/10.1007/s00126-020-01017-0

833 Dewaele, S., Muchez, Ph., Vets, J., Fernandez-Alonzo, M., Tack, L., 2006. Multiphase origin
834             of the Cu–Co ore deposits in the western part of the Lufilian fold-and-thrust belt,
835             Katanga (Democratic Republic of Congo). Journal of African Earth Sciences 46, 455–
836             469. https://doi.org/10.1016/j.jafrearsci.2006.08.002

837 Dewaide, L., Baele, J.-M., Collon-Drouaillet, P., Quinif, Y., Rochez, G., Vandycke, S., Hallet,
838             V., 2014. Karstification in dolomitized Waulsortian mudmounds (Belgium). Geologica
839             Belgica 17, 43–51.

840 du Dresnay, R., 1965. Notice géologique sur la région de Bou-Arfa – Colloque sur les gîtes
841             stratiformes de plomb, zinc et manganèse du Maroc (2 mai - 14 mai 1962). Notes et
842             Mémoires du Service Géologique du Maroc 181, 107–112.

843 El Desouky, H.A., Muchez, P., Cailteux, J., 2009. Two Cu–Co sulfide phases and contrasting
844             fluid systems in the Katanga Copperbelt, Democratic Republic of Congo. Ore
845             Geology Reviews 36, 315–332. https://doi.org/10.1016/j.oregeorev.2009.07.003

846 Fan, D., Yang, P., 1999. Introduction to and classification of manganese deposits of China.
847             Ore Geology Reviews 15, 1–13. https://doi.org/10.1016/S0169-1368(99)00011-6

848 Fan, D., Ye, J., Li, J., 1999. Geology, mineralogy, and geochemistry of the Middle
849             Proterozoic Wafangzi ferromanganese deposit, Liaoning Province, China. Ore
850             Geology Reviews 15, 31–53. https://doi.org/10.1016/S0169-1368(99)00013-X

851 Fleet, A.J., 1983. Hydrothermal and Hydrogenous Ferro-Manganese Deposits: Do They form
852             a Continuum? The Rare Earth Element Evidence, in: Rona, P.A., Boström, K.,
853             Laubier, L., Smith, K.L. (Eds.), Hydrothermal Processes at Seafloor Spreading
854             Centers. Springer US, Boston, MA, pp. 535–555. https://doi.org/10.1007/978-1-4899-
855             0402-7_23

856 Fleischer, M., Richmond, W.E., Evans, H.T., 1962. Studies of manganese oxides. 5.
857             Ramsdellite MnO2, an orthorhombic dimorph of pyrolusite. American Mineralogist 47,
858             47–58.

859 Folk, R.L., Chafetz, H.S., 2000. Bacterially Induced Microscale and Nanoscale Carbonate
860             Precipitates, in: Riding, R.E., Awramik, S.M. (Eds.), Microbial Sediments. Springer,
861             Berlin, Heidelberg, pp. 40–49. https://doi.org/10.1007/978-3-662-04036-2_6

862 Force, E.R., Back, W., Spiker, E.C., Knauth, L.P., 1986. A ground-water mixing model for the
863             origin of the Imini manganese deposit (Cretaceous) of Morocco. Economic Geology
864             81, 65–79. https://doi.org/10.2113/gsecongeo.81.1.65

865 Force, E.R., Cannon, W.F., 1988. Depositional model for shallow-marine manganese
866             deposits around black shale basins. Economic Geology 83, 93–117.
867             https://doi.org/10.2113/gsecongeo.83.1.93

868 Force, E.R., Maynard, J.B., 1991. Manganese: Syngenetic deposits on the margins of anoxic
869             basins, in: Sedimentary and Diagenetic Mineral Deposits: A Basin Analysis Approach
870             to Exploration. Society of Economic Geologists, Littleton, Colorado, pp. 147–159.

871 Frakes, L., Bolton, B.R., 1992. Effects of ocean chemistry, sea level, and climate on the
872             formation of primary sedimentary manganese ore deposits. Economic Geology 87,
873             1207–1217. https://doi.org/10.2113/gsecongeo.87.5.1207

874 Frizon de Lamotte, D., Leturmy, P., Missenard, Y., Khomsi, S., Ruiz, G., Saddiqi, O.,
875             Guillocheau, F., Michard, A., 2009. Mesozoic and Cenozoic vertical movements in the
876             Atlas system (Algeria, Morocco, Tunisia): An overview. Tectonophysics 475, 9–28.
877             https://doi.org/10.1016/j.tecto.2008.10.024

878 Frizon de Lamotte, D., Saint Bezar, B., Bracène, R., Mercier, E., 2000. The two main steps of
879             the Atlas building and geodynamics of the western Mediterranean. Tectonics 19,
880             740–761. https://doi.org/10.1029/2000TC900003

881 Froitzheim, N., 1984. Late Cretaceous vertical tectonics in the High Atlas SW of
882             Marrakech/Morocco - Reconstruction of tectonic movements in an early stage of the
883             High Atlas orogenesis. Neu Jb Paläont Mh 463–471.

884 Fu, Q., Qing, H., Bergman, K.M., 2006. Early dolomitization and recrystallization of carbonate
885             in an evaporite basin: the Middle Devonian Ratner laminite in southern

886            Saskatchewan, Canada. Journal of the Geological Society 163, 937–948.
887            https://doi.org/10.1144/0016-76492005-088

888 Gao, T., Fjellvåg, H., Norby, P., 2009. A comparison study on Raman scattering properties of
889            α- and β-$MnO_2$. Analytica Chimica Acta 648, 235–239.
890            https://doi.org/10.1016/j.aca.2009.06.059

891 Gasparrinia, M., Bakker, R.J., Bechstddt, Th., Boni, M., 2003. Hot dolomites in a Variscan
892            foreland belt: hydrothermal flow in the Cantabrian Zone (NW Spain). Journal of
893            Geochemical Exploration, Proceedings of Geofluids IV 78–79, 501–507.
894            https://doi.org/10.1016/S0375-6742(03)00115-8

895 Gaudefroy, G., 1960. Caractères distinctifs de la pyrolusite - ex manganite (application au
896            minerai de l'Imini). Notes du Service Géologique Marocain 19, 77–86.

897 Glasby, G.P., 2006. Manganese: Predominant Role of Nodules and Crusts, in: Schulz, H.D.,
898            Zabel, M. (Eds.), Marine Geochemistry. Springer-Verlag, Berlin/Heidelberg, pp. 371–
899            427. https://doi.org/10.1007/3-540-32144-6_11

900 Gouiza, M., Charton, R., Bertotti, G., Andriessen, P., Storms, J.E.A., 2017. Post-Variscan
901            evolution of the Anti-Atlas belt of Morocco constrained from low-temperature
902            geochronology. International Journal of Earth Sciences 106, 593–616.
903            https://doi.org/10.1007/s00531-016-1325-0

904 Gualtieri, A.F., Venturelli, P., 1999. In situ study of the goethite-hematite phase
905            transformation by real time synchrotron powder diffraction. American Mineralogist 84,
906            895–904. https://doi.org/10.2138/am-1999-5-624

907 Gutzmer, J., Beukes, N.J., 1996. Mineral paragenesis of the Kalahari managanese field,
908            South Africa. Ore Geology Reviews 11, 405–428. https://doi.org/10.1016/S0169-
909            1368(96)00011-X

910 Gutzmer, J., Beukes, N.J., Kleyenstuber, A.S.E., Burger, A.M., 1995. Magnetic hausmannite
911            from hydrothermally altered manganese ore in the Palaeoproterozoic Kalahari
912            manganese deposit, Transvaal Supergroup, South Africa. Mineralogical Magazine 59,
913            703–716. https://doi.org/10.1180/minmag.1995.059.397.12

914 Gutzmer, J., Beukes, N.J., Rhalmi, M., Mukhopadhyay, J., 2006. Cretaceous karstic cave-fill
915            manganese-lead-barium deposits of Imini, Morocco. Economic Geology 101, 385–
916            405. https://doi.org/10.2113/gsecongeo.101.2.385

917 Hewett, D.F., 1972. Manganite, hausmannite, braunite: features, modes of origin. Economic
918            Geology 67, 83–102. https://doi.org/10.2113/gsecongeo.67.1.83

919 Hoy, L.D., Ohmoto, H., 1989. Constraints for the genesis of redbed associated stratiform Cu
920            deposits from sulphur and carbon mass balance relations, in: Boyle, R.W., Brown,
921            A.C., Jefferson, C.W., Jowett, E.C., Kirkham, R.V. (Eds.), Sediment-Hosted Stratiform
922            Copper Deposits. St. John's, pp. 135–149.

923 Jébrak, M., Marcoux, É., Nasloubi, M., Zaharaoui, M., 1998. From sandstone- to carbonate-
924            hosted stratabound deposits: an isotope study of galena in the Upper-Moulouya
925            District (Morocco). Mineral. Deposita 33, 406–415.
926            https://doi.org/10.1007/s001260050158

927 Johnson, J.E., Webb, S.M., Ma, C., Fischer, W.W., 2016. Manganese mineralogy and
928            diagenesis in the sedimentary rock record. Geochimica et Cosmochimica Acta 173,
929            210–231. https://doi.org/10.1016/j.gca.2015.10.027

930 Jones, B., Renaut, R.W., 1994. Crystal fabrics and microbiota in large pisoliths from Laguna
931            Pastos Grandes, Bolivia. Sedimentology 41, 1171–1202.
932            https://doi.org/10.1111/j.1365-3091.1994.tb01448.x

933 Julien, C., Massot, M., Rangan, S., Lemal, M., Guyomard, D., 2002. Study of structural
934            defects in γ-$MnO_2$ by Raman spectroscopy. Journal of Raman Spectroscopy 33,
935            223–228. https://doi.org/10.1002/jrs.838

936 Julien, C.M., Massot, M., Poinsignon, C., 2004. Lattice vibrations of manganese oxides: Part
937            I. Periodic structures. Spectrochimica Acta Part A: Molecular and Biomolecular
938            Spectroscopy 60, 689–700. https://doi.org/10.1016/S1386-1425(03)00279-8

Kuleshov, V., 2016. Isotope geochemistry: the origin and formation of manganese rocks and ores. Elsevier, Amsterdam Boston Heidelberg London New York Oxford Paris San Diego San Francisco Singapore Sydney Tokyo.

Kuleshov, V.N., 2011. Manganese deposits: Communication 1. Genetic models of manganese ore formation. Lithology and Mineral Resources 46, 473–493. https://doi.org/10.1134/S0024490211050038

Lafforgue, L., 2016. Place de la minéralisation de manganèse de Bouarfa dans l'évolution méso-cénozoique de l'oriental marocain (PhD). Université Paris Sud, Paris.

Land, L.S., 1985. The Origin of Massive Dolomite. Journal of Geological Education 33, 112–125. https://doi.org/10.5408/0022-1368-33.2.112

Langford, J.I., Wilson, A.J.C., 1978. Scherrer after sixty years: A survey and some new results in the determination of crystallite size. J Appl Cryst 11, 102–113. https://doi.org/10.1107/S0021889878012844

Laznicka, P., 1992. Manganese deposits in the global lithogenetic system: Quantitative approach. Ore Geology Reviews 7, 279–356. https://doi.org/10.1016/0169-1368(92)90013-B

Lee, Y.I., Friedman, G.M., 1987. Deep-burial dolomitization in the Ordovician Ellenburger Group carbonates, West Texas and southeastern New Mexico. Journal of Sedimentary Research 57, 544–557. https://doi.org/10.1306/212F8B8E-2B24-11D7-8648000102C1865D

Leprêtre, R., Missenard, Y., Barbarand, J., Gautheron, C., Jouvie, I., Saddiqi, O., 2018. Polyphased inversions of an intracontinental rift: case study of the Marrakech High Atlas, Morocco. Tectonics 37, 818–841. https://doi.org/10.1002/2017TC004693

Leprêtre, R., Missenard, Y., Saint-Bezar, B., Barbarand, J., Delpech, G., Yans, J., Dekoninck, A., Saddiqi, O., 2015. The three main steps of the Marrakech High Atlas building in Morocco: Structural evidences from the southern foreland, Imini area. Journal of African Earth Sciences 109, 177–194. https://doi.org/10.1016/j.jafrearsci.2015.05.013

Lima-de-Faria, J., 1963. Dehydration of goethite and diaspore. Zeitschrift für Kristallographie - Crystalline Materials 119, 176–203. https://doi.org/10.1524/zkri.1963.119.3-4.176

Machel, H.G., 2004. Concepts and models of dolomitization: a critical reappraisal. Geological Society, London, Special Publications 235, 7–63. https://doi.org/10.1144/GSL.SP.2004.235.01.02

Machel, H.G., 2000. Application of Cathodoluminescence to Carbonate Diagenesis, in: Pagel, M., Barbin, V., Blanc, P., Ohnenstetter, D. (Eds.), Cathodoluminescence in Geosciences. Springer Berlin Heidelberg, Berlin, Heidelberg, pp. 271–301. https://doi.org/10.1007/978-3-662-04086-7_11

Manceau, A., Lanson, M., Takahashi, Y., 2014. Mineralogy and crystal chemistry of Mn, Fe, Co, Ni, and Cu in a deep-sea Pacific polymetallic nodule. American Mineralogist 99, 2068–2083. https://doi.org/10.2138/am-2014-4742

Mandernack, K.W., Fogel, M.L., Tebo, B.M., Usui, A., 1995a. Oxygen isotope analyses of chemically and microbially produced manganese oxides and manganates. Geochimica et Cosmochimica Acta 59, 4409–4425. https://doi.org/10.1016/0016-7037(95)00299-F

Mandernack, K.W., Post, J., Tebo, B.M., 1995b. Manganese mineral formation by bacterial spores of the marine Bacillus, strain SG-1: Evidence for the direct oxidation of Mn(II) to Mn(IV). Geochimica et Cosmochimica Acta 59, 4393–4408. https://doi.org/10.1016/0016-7037(95)00298-E

Mattauer, M., Tapponnier, P., Proust, F., 1977. Sur les mecanismes de formation des chaines intracontinentales; l'exemple des chaines atlasiques du Maroc. Bulletin de la Société Géologique de France S7-XIX, 521–526. https://doi.org/10.2113/gssgfbull.S7-XIX.3.521

Mauger, C.L., Compton, J.S., 2011. Formation of modern dolomite in hypersaline pans of the Western Cape, South Africa. Sedimentology 58, 1678–1692. https://doi.org/10.1111/j.1365-3091.2011.01229.x

994 Maynard, J.B., 2014. Manganiferous sediments, rocks, and ores, in: Treatise on
995     Geochemistry. Elsevier, pp. 327–349.

996 Maynard, J.B., 2010. The chemistry of manganese ores through time: a signal of increasing
997     diversity of earth-surface environments. Economic Geology 105, 535–552.
998     https://doi.org/10.2113/gsecongeo.105.3.535

999 Meister, P., Reyes, C., 2019. The Carbon-Isotope Record of the Sub-Seafloor Biosphere.
1000     Geosciences 9, 507. https://doi.org/10.3390/geosciences9120507

1001 Michard, A., Raddi, Y., 2011. Le manganèse de Bou-Arfa (Haut Atlas oriental), in: Mouttaqi,
1002     A., Rjimati, E.C., Maacha, L., Michard, André, Soulaimani, A., Ibouh, H. (Eds.), Les
1003     Principales Mines Du Maroc, Notes et Mémoires Du Service Géologique. Notes et
1004     mémoires du service géologique, Rabat, pp. 305–308.

1005 Missenard, Y., Saddiqi, O., Barbarand, J., Leturmy, P., Ruiz, G., El Haimer, F.-Z., Frizon de
1006     Lamotte, D., 2008. Cenozoic denudation in the Marrakech High Atlas, Morocco:
1007     insight from apatite fission-track thermochronology. Terra Nova 20, 221–228.
1008     https://doi.org/10.1111/j.1365-3121.2008.00810.x

1009 Missenard, Y., Zeyen, H., Frizon de Lamotte, D., Leturmy, P., Petit, C., Sébrier, M., Saddiqi,
1010     O., 2006. Crustal versus asthenospheric origin of relief of the Atlas Mountains of
1011     Morocco. Journal of Geophysical Research: Solid Earth 111, n/a-n/a.
1012     https://doi.org/10.1029/2005JB003708

1013 Montanez, I.P., Read, J.F., 1992. Fluid-rock interaction history during stabilization of early
1014     dolomites, upper Knox Group (Lower Ordovician), U.S. Appalachians. Journal of
1015     Sedimentary Research 62, 753–778. https://doi.org/10.1306/D42679D3-2B26-11D7-
1016     8648000102C1865D

1017 Mouttaqi, A., Rjimati, E.C., Maacha, L., Michard, A., Soulaimani, A., Ibouh, H., 2011. Les
1018     principales mines du Maroc, Editions du Service Géologique du Maroc. ed, New
1019     geological and mining guidebooks of Morocco. Ministère de l'Energie, des Mines, de
1020     l'Eau et de l'Environnement, Rabat.

1021 Nader, F.H., Swennen, R., Ellam, R.M., 2006. Petrographic and geochemical study of
1022     Jurassic dolostones from Lebanon: Evidence for superimposed diagenetic events.
1023     Journal of Geochemical Exploration, GEOFLUIDS V: 5th International Conference on
1024     Fluid Evolution, Migration and Interaction in Sedimentary Basins and Orogenic Belts
1025     89, 288–292. https://doi.org/10.1016/j.gexplo.2005.11.003

1026 Nader, F.H., Swennen, R., Ellam, R.M., Immenhauser, A., 2007. Field geometry, petrography
1027     and geochemistry of a dolomitization front (Late Jurassic, central Lebanon).
1028     Sedimentology 54, 1093–1120. https://doi.org/10.1111/j.1365-3091.2007.00874.x

1029 Nicholson, K., 1992. Contrasting mineralogical-geochemical signatures of manganese
1030     oxides; guides to metallogenesis. Economic Geology 87, 1253–1264.
1031     https://doi.org/10.2113/gsecongeo.87.5.1253

1032 Nottvedt, A., Gabrielsen, R.H., Steel, R.J., 1995. Tectonostratigraphy and sedimentary
1033     architecture of rift basins, with reference to the northern North Sea. Marine and
1034     Petroleum Geology, Integrated Basin Studies 12, 881–901.
1035     https://doi.org/10.1016/0264-8172(95)98853-W

1036 Okita, P.M., Maynard, J.B., Spiker, E.C., Force, E.R., 1988. Isotopic evidence for organic
1037     matter oxidation by manganese reduction in the formation of stratiform manganese
1038     carbonate ore. Geochimica et Cosmochimica Acta 52, 2679–2685.
1039     https://doi.org/10.1016/0016-7037(88)90036-1

1040 Ostwald, J., 1992. Genesis and paragenesis of the tetravalent manganese oxides of the
1041     Australian continent. Economic Geology 87, 1237–1252.
1042     https://doi.org/10.2113/gsecongeo.87.5.1237

1043 Ostwald, J., 1990. The biogeochemical origin of the Groote Eylandt manganese oxide
1044     pisoliths and ooliths, northern Australia. Ore Geology Reviews, Palynology of ore
1045     deposits 5, 469–490. https://doi.org/10.1016/0169-1368(90)90048-R

1046 Pasero, M., 2005. A Short Outline of the Tunnel Oxides. Reviews in Mineralogy and
1047     Geochemistry 57, 291–305. https://doi.org/10.2138/rmg.2005.57.9

1048 Pierce, M.L., Moore, C.B., 1982. Adsorption of arsenite and arsenate on amorphous iron
1049    hydroxide. Water Research 16, 1247–1253. https://doi.org/10.1016/0043-
1050    1354(82)90143-9

1051 Piqué, A., Charroud, M., Laville, E., Ait Brahim, L., Amrhar, M., 2000. The Tethys southern
1052    margin in Morocco; Mesozoic and Caenozoic evolution of the Atlas domain, in:
1053    Crasquin-Soleau, S., Barrier, E. (Eds.), New Data on Peri-Tethyan Sedimentary
1054    Basins. Publications scientifiques du Muséum, Paris, pp. 93–106.

1055 Polgári, M., Hein, J.R., Vigh, T., Szabó-Drubina, M., Fórizs, I., Bíró, L., Müller, A., Tóth, A.L.,
1056    2012. Microbial processes and the origin of the Úrkút manganese deposit, Hungary.
1057    Ore Geology Reviews 47, 87–109. https://doi.org/10.1016/j.oregeorev.2011.10.001

1058 Polgári, M., Okita, P.M., Hein, J.R., 1991. Stable Isotope evidence for the origin of the Urkut
1059    Manganese ore deposit, Hungary. SEPM Journal of Sedimentary Research 61.
1060    https://doi.org/10.1306/D426771C-2B26-11D7-8648000102C1865D

1061 Pomiès, M.P., Morin, G., Vignaud, C., 1998. XRD study of the goethite-hematite
1062    transformation: Application to the identification of heated prehistoric pigments.
1063    European Journal of Solid State and Inorganic Chemistry 35, 9–25.
1064    https://doi.org/10.1016/S0992-4361(98)80011-8

1065 Poot, J., Verhaert, M., Dekoninck, A., Oummouch, A., El Basbas, A., Maacha, L., Yans, J.,
1066    2020. Characterization of Weathering Processes of the Giant Copper Deposit of
1067    Tizert (Igherm Inlier, Anti-Atlas, Morocco). Minerals 10, 620.
1068    https://doi.org/10.3390/min10070620

1069 Post, J.E., 1999. Manganese oxide minerals: crystal structures and economic and
1070    environmental significance. Proceedings of the National Academy of Sciences 96,
1071    3447–3454. https://doi.org/10.1073/pnas.96.7.3447

1072 Post, J.E., Heaney, P.J., Hanson, J., 2003. Synchrotron X-ray diffraction study of the
1073    structure and dehydration behavior of todorokite. American Mineralogist 88, 142–150.
1074    https://doi.org/10.2138/am-2003-0117

1075 Pouit, G., 1980. Manganèse. Notes et Mémoires du Service Géologique du Maroc, Rabat 13,
1076    61–67.

1077 Pouit, G., 1964. Les gîtes de manganèse marocains encaissés dans les Formations
1078    carbonatées : éléments pour une synthèse. Chronique des Mines et de la Recherche
1079    Minière 371–380.

1080 Pouit, G., Jouravsky, G., 1965. Les minéralisations manganésifères de la région de Bou-Arfa
1081    - Colloque sur les gites stratiformes de plomb, zinc, et manganèse du Maroc. Notes
1082    et Mémoires du Service Géologique du Maroc 181, 113–131.

1083 Radke, B.M., Mathis, R.L., 1980. On the formation and occurrence of saddle dolomite.
1084    Journal of Sedimentary Research 50, 1149–1168. https://doi.org/10.1306/212F7B9E-
1085    2B24-11D7-8648000102C1865D

1086 Rddad, L., 2021. The genesis of the Jurassic-hosted Mississippi Valley-type Pb-Zn ore
1087    deposit, Tigrinine-Taabast district (Central High Atlas, Morocco): Insights from fluid
1088    inclusion and C-O-S-Pb isotope studies. Journal of African Earth Sciences 174,
1089    104071. https://doi.org/10.1016/j.jafrearsci.2020.104071

1090 Rddad, L., Bouhlel, S., 2016. The Bou Dahar Jurassic carbonate-hosted Pb–Zn–Ba deposits
1091    (Oriental High Atlas, Morocco): Fluid-inclusion and C–O–S–Pb isotope studies. Ore
1092    Geology Reviews 72, 1072–1087. https://doi.org/10.1016/j.oregeorev.2015.08.011

1093 Rddad, L., Mouguina, E.M., Muchez, P., Darling, R.S., 2018. The genesis of the Ali Ou
1094    Daoud Jurassic carbonate Zn-Pb Mississippi Valley-type deposit, Moroccan central
1095    High Atlas: Constraints from bulk stable C-O-S, in situ radiogenic Pb isotopes, and
1096    fluid inclusion studies. Ore Geology Reviews 99, 365–379.
1097    https://doi.org/10.1016/j.oregeorev.2018.06.020

1098 Ren, M., Jones, B., 2017. Spatial variations in the stoichiometry and geochemistry of
1099    Miocene dolomite from Grand Cayman: Implications for the origin of island dolostone.
1100    Sedimentary Geology 348, 69–93. https://doi.org/10.1016/j.sedgeo.2016.12.001

Rendon, J.L., Cornejo, J., de Arambarri, P., 1983. Grinding-induced effects on goethite (α-FeOOH). Journal of Colloid and Interface Science 94, 546–551. https://doi.org/10.1016/0021-9797(83)90294-1

Roy, S., 2006. Sedimentary manganese metallogenesis in response to the evolution of the Earth system. Earth-Science Reviews 77, 273–305. https://doi.org/10.1016/j.earscirev.2006.03.004

Salahane, A., 1978. Etude géologique et métallogénique du gisement cuprifère du Jbel Klakh Haut Atlas oriental (Maroc): Contribution à la métallogénie paléokarstique. Notes et Mémoires du Service Géologique du Maroc 40, 147–237.

Scherrer, P., 1918. Estimation of the size and internal structure of colloidal particles by means of röntgen. Nachrichten von der Gesellschaft der Wissenschaftenzu Göttingen Mathematisch-Physikalische Klasse, 2, 96–100.

Schwertmann, U., Cambier, P., Murad, E., 1985. Properties of Goethites of Varying Crystallinity. Clays Clay Miner. 33, 369–378. https://doi.org/10.1346/CCMN.1985.0330501

Searl, A., 1989. Saddle dolomite: a new view of its nature and origin. Mineralogical Magazine 53, 547–555. https://doi.org/10.1180/minmag.1989.053.373.05

Searl, A., Fallick, A.E., 1990. Dinantian dolomites from East Fife: hydrothermal overprinting of early mixing-zone stable isotopic and Fe/Mn compositions. Journal of the Geological Society 147, 623–638. https://doi.org/10.1144/gsjgs.147.4.0623

Seber, D., Barazangi, M., Tadili, B.A., Ramdani, M., Ibenbrahim, A., Ben Sari, D., 1996. Three-dimensional upper mantle structure beneath the intraplate Atlas and interplate Rif mountains of Morocco. Journal of Geophysical Research: Solid Earth 101, 3125–3138. https://doi.org/10.1029/95JB03112

Teixell, A., Bertotti, G., de Lamotte, D.F., Charroud, M., 2009. The geology of vertical movements of the lithosphere: An overview. Tectonophysics 475, 1–8. https://doi.org/10.1016/j.tecto.2009.08.018

Torres-Ruiz, J., 1983. Genesis and evolution of the Marquesado and adjacent iron ore deposits, Granada, Spain. Economic Geology 78, 1657–1673. https://doi.org/10.2113/gsecongeo.78.8.1657

Varentsov, I.M., 1996. Manganese ores of supergene zone: Geochemistry of formation, Solid Earth Sciences Library. Springer Netherlands, Dordrecht.

Verhaert, M., Bernard, A., Dekoninck, A., Lafforgue, L., Saddiqi, O., Yans, J., 2017. Mineralogical and geochemical characterization of supergene Cu–Pb–Zn–V ores in the Oriental High Atlas, Morocco. Mineralium Deposita. https://doi.org/10.1007/s00126-017-0753-5

Verhaert, M., Bernard, A., Saddiqi, O., Dekoninck, A., Essalhi, M., Yans, J., 2018. Mineralogy and Genesis of the Polymetallic and Polyphased Low Grade Fe-Mn-Cu Ore of Jbel Rhals Deposit (Eastern High Atlas, Morocco). Minerals 8, 39. https://doi.org/10.3390/min8020039

Walter, D., Buxbaum, G., Laqua, W., 2001. The Mechanism of the Thermal Transformation From Goethite to Hematite. Journal of Thermal Analysis and Calorimetry 63, 733–748. https://doi.org/10.1023/A:1010187921227

Wang, X., Müller, W.E.G., 2009. Marine biominerals: perspectives and challenges for polymetallic nodules and crusts. Trends in Biotechnology 27, 375–383. https://doi.org/10.1016/j.tibtech.2009.03.004

Warren, J., 2000. Dolomite: occurrence, evolution and economically important associations. Earth-Science Reviews 52, 1–81. https://doi.org/10.1016/S0012-8252(00)00022-2

White, N., McKenzie, D., 1988. Formation of the steer's head geometry of sedimentary basins by differential stretching of the crust and mantle. Geology 16, 250–253. https://doi.org/10.1130/0091-7613(1988)016<0250:FOTSSH>2.3.CO;2

Wolska, E., Schwertmann, U., 1989. Nonstoichiometric structures during dehydroxylation of goethite. Zeitschrift für Kristallographie - Crystalline Materials 189, 223–237. https://doi.org/10.1524/zkri.1989.189.3-4.223

Wolska, E., Szajda, W., 1988. The effect of cationic and anionic substitution on the α-(Al, Fe)2O3 lattice parameters. Solid State Ionics 28–30, 1320–1323. https://doi.org/10.1016/0167-2738(88)90379-7

Yelles-Chaouche, A.K., Ait Ouali, R., Bracene, R., Derder, M.E.M., Djellit, H., 2001. Chronologie de l'ouverture du bassin des Ksour (Atlas Saharien, Algerie) au debut du Mesozoique. Bulletin de la Société Géologique de France 172, 285–293. https://doi.org/10.2113/172.3.285

Yoshino, T., Miura, H., Hariya, Y., 1993. Crystal structure of orthorhombic pyrolusite from Imini mine, in: Ishihara, S., Urabe, T., Ohmoto, H. (Eds.), Mineral Resources Symposia. Society of Resource Geologists of Japan, Tokyo, pp. 62–65.

Yoshino, T., Miura, H., Hariya, Y., 1992. Crystal structure of orthorhombic pyrolusite, in: Abstract Book. Presented at the International Geological Congress, Kyoto, p. 216.

Zenger, D.H., Dunham, J.B., Ethington, R.L. (Eds.), 1980. Concepts and Models of Dolomitization. SEPM (Society for Sedimentary Geology). https://doi.org/10.2110/pec.80.28

Zwicker, W.K., Groeneveld-Meijer, W.O.J., Jaffe, H.W., 1962. Nsutite - a widespread manganese oxide mineral. American Mineralogist 47, 618–623.

**Figures**

**Fig. 1 (color). A.** Simplified structural map of Morocco showing the location of Mn mineralization. MA= Middle Atlas, EHA=Eastern High Atlas, HA= High Atlas, WHA=Western High Atlas, SAF=South Atlas Front, NAF=North Atlas Front. **B**. Local geological map of the Bou Arfa cliff and the Mn mineralization (modified after Pouit and Jouravsky 1965). H1-4=Hamaraouet, HB=Hamarouet and Aïn Beida, 63= Gallery 63.

**Fig. 2 (black and white).** Stratigraphic column of the Tamlet area (left) and in the Hamaraouet sector (right).

**Fig. 3 (color).** Petrographic views of carbonate generations in the host rock. **A.** CL view of a sandstone level at the base of the UCU cemented by Dol-1a (sample J2-2). **B.** Oolith replaced by Dol-1a and cemented by Dol-1b under CL at the bottom of the UCU. **C.** Successive generations of dolomite crystals filling fractures and void in H2 (sample H2 – Dol – Min). **D.** Bird eyes facies in the UCU dolostone at Hamaraouet (H1) crisscrossed by several calcite veins. **E.** Dedolomitization of Dol-2A in the Mn ore at Hamaraouet (H3) with pyrolusite crystals. **F.** Late calcite filling void at Hamaraouet (sample H2-Br-Dol). **G.** Early dolomite generation with ferrous (Cal-1a) and non-ferrous (Cal-1b) calcites in the UCU of the Jbel Bou Moktha under PPL prepared with a mix of alizarine-red and K-ferricyanide. **H.** Late calcite generations in the UCU of Jbel Bou Moktha under CL. Dol=dolomite, Py=pyrolusite, Ca=calcite.

**Fig. 4 (color).** Tentative paragenetic sequence of the Bou Arfa deposit. Schematic petrographic reconstruction of dolomite generations is given for cement and veins (see Table 6 for key features of dolomite generations).

31

**Fig. 5 (color).** Field observations of the Mn and Fe ores. See location on Fig. 1B. **A.** Galleries in the Hamaraouet area (H1) in the Upper "Chocolate" Unit. **B.** View of the Aïn Beida mining site and the Bou Arfa cliff. **C.** Stratabound orebody in gallery 63. **D.** Stockwork in the host UCU dolostone between Aïn Beida and Hamaraouet (HB). **E.** Mn and Fe oxides in the Hamaraouet area (H1). **F.** Massive goethite vein in the Hamaraouet area (H3). **G.** Fe oxide vein crossing the stratabound Mn ore in gallery 63. **H.** Stockwork of pyrolusite in the UCU in Hamaraouet (H3).

**Fig. 6 (color).** Petrographic views of main mineralization types. **A.** Cluster mineralization showing pyrolusite veins crossing early dolomite generation (Dol-1 and 2) filled by calcite under SEM-BSE view at Hamaraouet. **B.** Disseminated bipyramidal pyrolusite growing onto altered Dol-2B and cemented by coarse Dol-3B under SEM-BSE view at H2 (sample H2-Dol-Min). **C.** Cluster mineralization showing needles and fusiform pyrolusite in gallery 63 under NAPL. **D.** Raman spectra for pyrolusite in gallery 63 (63-01_3D1, 63-01_2D1) and between Hamaraouet and Aïn Beida (HA; HAB_1D1). **E.** Pyrolusite growing onto early botryoidal goethite generation in gallery 63 under NAPL. **F.** Pyrolusite and cryptomelane crossing hausmannite crystals and Dol-3 under SEM-BSE view at Hamaraouet (H1-Min2). Hausmannite is partly weathered into chalcophanite. Note that pyrolusite, in turn, seems to partly weathers into cryptomelane. **G.** Late botryoidal goethite brecciated by Dol-3A generation under SEM-BSE view at Hamaraouet. Note that late goethite grows onto the pyrolusite-calcite matrix. **H.** SEM-BSE view of hausmannite filled by Dol-3b and pyrolusite. Hollandite partly replaces pyrolusite. Dol=dolomite, Cal=calcite, Py=pyrolusite, Cph=chalcophanite, Hs=hausmannite, Cry=cryptomelane, Gth=goethite, Hol=hollandite.

**Fig. 7 (color).** Petrographic views of main mineralization types. **A.** Mixing of different Mn oxides (hausmannite, pyrolusite, cryptomelane, chalcophanite) within the host dolostone in Hamaraouet (H1) under PPL. **B.** Zoom of Fig. 6A under SEM-BSE showing hausmannite replaced by chalcophanite and cryptomelane. Pyrolusite occurs between hausmannite crystals. Note that Dol-3 is broken by cryptomelane. **C.** SEM-BSE view showing phase relation between hausmannite and manganite crossed by Mn carbonate (Ca-rhodochrosite) at Aïn Beida (AB). **D.** SEM-BSE view of crest-like barite associated with manganite and late Mn carbonate at Aïn Beida (AB). **E.** Massive late goethite generation growing onto hummocky pyrolusite in Hamaraouet (H4). Dol=dolomite, Cal=calcite, Py=pyrolusite, Cph=chalcophanite, Hs=hausmannite, Cry=cryptomelane, Gth=goethite, Mnt=manganite, Ba=barite, Rh=rhodochrosite.

**Fig. 8 (black and white).** Average integral crystallites of goethite (A) and hematite (B) samples.

**Fig. 9 (color).** Geochemistry of dolomite generations (Table 4). **A.** Composition of cement dolomite in the host rock. **B.** Composition of vein-filling dolomite. **C.** Distribution of MnO and FeO of dolomite in various geological settings. The Bou Arfa dolomite generations display an individual trend toward low FeO/MnO ratio.

**Fig. 10 (color).** Trace element pattern of whole rock analyses in the Mn (A) and Fe (B) ores (Tables 2 and 3).

**Fig. 11 (color).** Stable isotope (Table 7) plot to show the trend of progressive dolomitization in the Bou Arfa Mn deposit. Data from MVT deposits (Bouabdellah et al., 2012; Rddad, 2021; Rddad et al., 2018; Rddad and Bouhlel, 2016), Mn Imini deposit (Force et al., 1986) and shallow Mn-rich dolomite (Burns and Baker, 1987) are included.

**Fig. 12 (black and white). A.** PCA statistical distribution of chemical elements in the Bou Arfa deposit. **B-C.** Discrimination plot (Nicholson, 1992) between hydrothermal, supergene and dubhite Mn accumulation.

**TABLES**

**Table 1.** Description and location (Fig. 1B) of the studied samples. The mineralogy is referred as Qz=quartz, Fds=feldspars, Zr=zircon, Ap=apatite, Musc=muscovite, Dol=dolomite, Bt=biotite, Fe-Ti Ox.= Fe-Ti oxides, Py=pyrolusite, Hs=hausmannite, Fe-ox= Fe oxyhydroxides, Cph=chalcophanite, Cpm=cryptomelane, Cal=calcite, Hem=hematite, Goe=goethite, Hol=hollandite, Ba=barite. The main minerals are in bolt. WRA is the whole rock analysis.

**Table 2.** Whole rock geochemistry (major and trace elements) of the host and basement rocks given in wt.% (major oxides and LOI) and ppm (traces). <D.L. is under detection limit. LOI is the lost on ignition.

**Table 3.** Whole rock geochemistry (major and trace elements) of the Mn and Fe ores rocks given in wt.% (major oxides and LOI) and ppm (traces). <D.L. is under detection limit. LOI is the lost on ignition.

**Table 4.** EPMA analyses of different carbonate phases. The average values are given with their minimum (min) and maximum (max) values. The number of analyses is mentioned (=n). Standard deviation is also indicated for each batch and for the instrument ($\sigma$). D.L. is the detection limit. Standard list can be found in the data repository.

**Table 5.** EPMA analyses of Mn oxides: hausmannite and pyrolusite in Hamaraouet, and supergene cryptomelane, hollandite and chalcophanite. The number of analyses is

1262 mentioned (=n). The average values are given. Standard deviation is also indicated for each
1263 batch and for the instrument (σ). D.L. is the detection limit. Standard list can be found in the
1264 data repository. Standard list can be found in the data repository.

1265 **Table 6.** EPMA analyses of different Fe oxides. The number of analyses is mentioned (=n).
1266 The average values are given. Standard deviation is also indicated for each batch and for the
1267 instrument (σ). D.L. is the detection limit. Standard list can be found in the data repository.

1268 **Table 7.** $\delta^{13}C$ and $\delta^{18}O$ compositions of dolomite in the Bou Arfa deposit. See Fig. 1B for the
1269 location of the studied samples.

1270 **Table 8.** Key identification criteria of the dolomite generations under cathodoluminescence
1271 (CL)and light microscopy (LM).

1272 **Table 9.** Cell dimensions of four goethite in Hamaraouet (Fig. 2) following the three main cell
1273 orthorhombic axis. The error is calculated according to the deviation of the experimental
1274 peak from the standard value.

1276 **Supplementary data repository**

1277 **DR1.** Analytical conditions standards of the EPMA CAMECA SX-five analyses.

1278 **DR2.** Peak features in the XRD patterns of botryoidal hematite (H3_Hem) and across the
1279 massive goethite vein (H3_Gth6-9).

1280 Highlights

1281 • The Bou Arfa Mn(-Fe) mineralization (High Atlas, Morocco) is formed by post-
1282 sedimentary processes
1283 • Dolomitization is considered as the main driver for Mn and Fe concentration
1284 • The stability of the Mn(-Fe)-bearing minerals disabled strong post-ore weathering
1285 • The proposed metallogenic model is similar to the genesis of Atlasic MVT deposits

1286